

DISCOVERY OF EXTREME [OIII] $\lambda$ 5007Å OUTFLOWS IN HIGH-REDSHIFT RED QUASARSNADIA L. ZAKAMSKA<sup>1</sup>, FRED HAMANN<sup>2</sup>, ISABELLE PÂRIS<sup>3</sup>, W. N. BRANDT<sup>4</sup>, JENNY E. GREENE<sup>5</sup>, MICHAEL A. STRAUSS<sup>5</sup>, CAROLIN VILLFORTH<sup>6,7</sup>, DOMINIKA WYLEZALEK<sup>1</sup>, RACHAEL M. ALEXANDROFF<sup>1</sup>, NICHOLAS P. ROSS<sup>8</sup>*Draft version Thursday 16<sup>th</sup> May, 2019*

## ABSTRACT

Black hole feedback is now a standard component of galaxy formation models. These models predict that the impact of black hole activity on its host galaxy likely peaked at  $z = 2-3$ , the epoch of strongest star formation activity and black hole accretion activity in the Universe. We used XShooter on the Very Large Telescope to measure rest-frame optical spectra of four  $z \sim 2.5$  extremely red quasars with infrared luminosities  $\sim 10^{47}$  erg s<sup>-1</sup>. We present the discovery of very broad (full width at half max = 2600 – 5000 km s<sup>-1</sup>), strongly blue-shifted (by up to 1500 km s<sup>-1</sup>) [OIII] $\lambda$ 5007Å emission lines in these objects. In a large sample of obscured and red quasars, [OIII] kinematics are positively correlated with infrared luminosity, and the four objects in our sample are on the extreme end both in [OIII] kinematics and infrared luminosity. We estimate that 3% of the bolometric luminosity in these objects is being converted into the kinetic power of the observed wind. These sources may be the signposts of the most extreme form of quasar feedback at the peak epoch of galaxy formation, and may represent an active “blow-out” phase of quasar evolution.

*Subject headings:* galaxies: evolution – quasars: emission lines – quasars: general

## 1. INTRODUCTION

While supermassive black holes have masses only  $\sim 0.1\%$  of their host galaxies, they are now thought to exert a significant controlling effect on galaxy evolution (Tabor & Binney 1993; Silk & Rees 1998; Springel et al. 2005). The enormous power of the relativistic outflows and the radiation from the accretion disk may be the critical agent limiting the mass of galaxies in the Universe (Thoul & Weinberg 1995; Croton et al. 2006). At the same time, the strong correlations between black hole masses and the velocity dispersions of their hosts in the present-day universe (Gebhardt et al. 2000; Ferrarese & Merritt 2000; Gültekin et al. 2009) and the similarity of the cosmic evolution of star formation and black hole accretion (Boyle & Terlevich 1998; Hopkins et al. 2008; Madau & Dickinson 2014) also suggest a connection between the formation of supermassive

black holes and their host galaxies.

One possibility for such a connection, known as “quasar feedback”, is that the energy output of the black hole in its most luminous (quasar) phase becomes coupled to the gas from which stars in the host galaxy would otherwise form. The gas is then reheated or pushed out of the galactic potential (Hopkins et al. 2006), resulting in suppression of star formation and in a “quenched” galaxy. Just like the winds driven by powerful starbursts (Heckman et al. 1990; Veilleux et al. 1994, 2005), such galaxy-wide quasar-driven winds are likely to be inhomogeneous, with different phases of the wind medium observable in different domains of the electromagnetic spectrum. As a result, observational evidence for quasar-driven winds has been accumulating via multiple different observational techniques which trace different components of the wind (e.g., Arav et al. 2008; Chartas et al. 2009; Nesvadba et al. 2010; Ogle et al. 2010; Rupke & Veilleux 2013a; Veilleux et al. 2013a; Tombesi et al. 2013; Greene et al. 2014a; Sun et al. 2014; Crichton et al. 2015; Nardini et al. 2015).

One fruitful technique is observations of forbidden emission lines of ionized gas. Because luminous quasars can easily ionize all the available gas over the entire galaxy and even into intergalactic space (Stockton & MacKenty 1987; Liu et al. 2009; Villar-Martín et al. 2011; Hainline et al. 2013), the large spatial extents of ionized gas by themselves do not constitute evidence for quasar feedback or a wind: very extended narrow line emission could simply be due to gas left-over from a merger event or even a small companion galaxy illuminated by the quasar.

Rather, a tell-tale sign of a galactic wind is the presence of strongly kinematically disturbed gas at large distances from the galactic center, as measured by spatially resolved long-slit and integral field unit observations (Nesvadba et al. 2006, 2008; Greene et al. 2011; Cano-Díaz et al. 2012; Liu et al.

<sup>1</sup> Department of Physics & Astronomy, Johns Hopkins University, Bloomberg Center, 3400 N. Charles St., Baltimore, MD 21218, USA

<sup>2</sup> Department of Astronomy, University of Florida, 32611 Gainesville, FL, USA

<sup>3</sup> LAM - Laboratoire d’Astrophysique de Marseille, Pôle de l’Étoile Site de Château-Gombert 38, rue Frédéric Joliot-Curie 13388 Marseille cedex 13, France

<sup>4</sup> Department of Astronomy & Astrophysics, 525 Davey Lab, The Pennsylvania State University, University Park, PA 16802, USA; Institute for Gravitation and the Cosmos, The Pennsylvania State University, University Park, PA 16802, USA; Department of Physics, 104 Davey Lab, The Pennsylvania State University, University Park, PA 16802, USA

<sup>5</sup> Department of Astrophysical Sciences, Princeton University, Princeton, NJ 08544, USA

<sup>6</sup> Scottish Universities Physics Alliance (SUPA), University of St Andrews, School of Physics and Astronomy, North Haugh, KY16 9SS, St Andrews, Fife, UK

<sup>7</sup> University of Bath, Department of Physics, Claverton Down, Bath, BA2 7AY, UK

<sup>8</sup> Scottish Universities Physics Alliance (SUPA), Institute for Astronomy, University of Edinburgh, Royal Observatory, Edinburgh EH9 3HJ, UK

2013a,b; Alexandroff et al. 2013; Rupke & Veilleux 2013b; Harrison et al. 2014; Zakamska & Greene 2014). Gas extended over a few kpc scales and moving with velocities of  $\gtrsim 1000 \text{ km s}^{-1}$  cannot be in dynamical equilibrium with the galaxy and cannot be confined by any realistic galactic potential. Even in the absence of spatial information, it is often assumed that in quasars forbidden line emission must be extended on scales of  $\gtrsim 1 \text{ kpc}$  because forbidden transitions arise in relatively low density ( $n$  from  $10 \text{ cm}^{-3}$  to a few  $\times 10^5 \text{ cm}^{-3}$ ) warm ( $T \sim 10^4 \text{ K}$ ) clouds. Therefore, very high velocity dispersions or strong line asymmetries in forbidden lines – especially blue-shifts which arise naturally in dusty winds (Whittle 1985a) – are sufficient evidence of high-velocity extended outflows (Spoon & Holt 2009; Mullaney et al. 2013; Zakamska & Greene 2014; Brusa et al. 2015).

The key epoch for studies of quasar feedback is that of peak star formation and quasar activity at redshifts  $z = 2 - 3$  (Boyle & Terlevich 1998; Hopkins et al. 2008): this is likely the epoch at which the modern-day relationships between black holes and their hosts were established, as massive galaxies grew most of their stellar mass at that time. In evolutionary models of quasar obscuration (Sanders et al. 1988; Hopkins et al. 2006) it is the obscured quasars which are most likely to be found in the strong feedback phase. Therefore, luminous reddened and obscured quasars at the peak galaxy formation epoch are promising locations to look for the most powerful quasar-driven winds. While obscured quasars remain difficult to find in large numbers at high redshifts because of their faintness in the rest-frame ultra-violet and optical, and often even at X-ray wavelengths, several samples have become recently available (Alexandroff et al. 2013; Eisenhardt et al. 2012; Tsai et al. 2015; Ross et al. 2015; Brusa et al. 2015).

In this paper we present a discovery of extreme ionized gas outflows in four luminous red quasars identified by Ross et al. (2015), which we will argue are a manifestation of strong quasar feedback. In Section 2 we describe our observations and data reduction. In Section 3 we analyze the kinematics and the strengths of the forbidden emission lines. In Section 4 we compare our results to those of other samples and discuss the possible role of such objects in galaxy evolution, and we conclude in Section 5. We use an  $h = 0.7$ ,  $\Omega_m = 0.3$ ,  $\Omega_\Lambda = 0.7$  cosmology. The sources are identified by their full hh-mmss.ss+ddmmss.s coordinates in Table 1 and shortened to SDSS Jhhmm+ddmm elsewhere. We use air wavelengths for emission-line identifications in the text, but because SDSS and VLT spectra are calibrated for vacuum wavelengths, in all calculations we use vacuum wavelengths of emission lines (e.g.,  $[\text{OIII}]\lambda 5007\text{\AA}$  has a laboratory wavelength of  $5008.24\text{\AA}$ ).

## 2. OBSERVATIONS AND DATA REDUCTION

The targets for this work are drawn from the sample of extremely red quasars by Ross et al. (2015). Briefly, in a search of red and obscured quasar candidates, Ross et al. (2015) selected objects classified as quasars in the Baryon Oscillation Spectroscopic Survey (BOSS; Dawson et al. 2013) of the Sloan Digital Sky Survey (SDSS; York et al. 2000; Eisenstein et al. 2011; Alam et al. 2015) database,

which also had extreme infrared-to-optical colors as measured by the SDSS and the Wide-field Infrared Survey Explorer (WISE; Wright et al. 2010). Out of 65 sources at the tail of the infrared-to-optical ratio distribution, most are, as expected, obscured or heavily reddened quasars, but about twelve objects defy simple explanations. These sources have rest-frame ultra-violet emission lines with the high rest equivalent widths (e.g.,  $\text{CIV}\lambda 1549\text{\AA}$  with  $\text{REW} > 200\text{\AA}$ ) expected in type 2 quasars where the continuum is strongly suppressed due to obscuration but lines arise in an extended region. However, the emission line velocity widths are  $> 2000 \text{ km s}^{-1}$ , which is typical of type 1 quasars, and emission lines often display bizarre shapes and line ratios not commonly seen in active nuclei of any known type. Specifically, these objects show high  $\text{NV}\lambda 1240\text{\AA}/\text{Ly}\alpha$  ratios and peculiar “stubby”  $\text{CIV}\lambda 1549\text{\AA}$  emission line profiles which lack the extended wings characteristic of lines in ordinary quasars (Figure 1).

We selected four such targets with infrared-to-optical ratios  $r_{\text{AB}} - W_{4\text{Vega}} > 14 \text{ mag}$  and with rest equivalent widths of  $\text{CIV}\lambda 1549\text{\AA}$  in excess of  $200\text{\AA}$  for observations (PI: I. Pâris) with the European Southern Observatory’s Very Large Telescope (VLT) using XShooter, a medium resolution spectrograph allowing simultaneous observations over the wavelength range from  $0.3$  to  $2.48\mu\text{m}$  (Vernet et al. 2011). In our upcoming analysis of the full VLT dataset (Hamann et al. in prep. 2016b) we will discuss the optical part of the VLT spectra and comparison of optical properties of quasars of different infrared-to-optical colors. In this paper we focus on the spectacular forbidden  $[\text{OIII}]\lambda\lambda 4959, 5007\text{\AA}$  emission lines discovered in the four red quasars using the near-infrared part of the VLT spectra. The BOSS spectra of the four targets discussed in this paper are shown in Figure 1. None of the objects are detected in the radio at  $1 \text{ mJy}$  level (Becker et al. 1995), implying that their radio luminosities are below  $\nu L_\nu[1.4\text{GHz}] \sim 5 \times 10^{41} \text{ erg s}^{-1}$  and that they can be considered radio-quiet.

We acquired near-infrared spectra with slit width of  $0.9''$ , resulting in a spectral resolution of  $R = 5100$  (Vernet et al. 2011). Our program was designed to have a homogeneous signal-to-noise across the sample based on the known optical fluxes. The total exposure time for brighter targets (SDSS J0834+0159 and SDSS J1232+0912) was 2400s, and it was 3600s for the fainter ones (SDSS J2215–0056 and SDSS J2323–0100). Data were acquired in service mode between 2nd April 2014 and 26th July 2014.

We reduced the data using a custom pipeline developed by George Becker and described in Lopez et al. (in prep.). It is based on the techniques of Kelson (2003) with all the steps computed on the unrectified two-dimensional frames. Each near-infrared frame was dark subtracted and flat-fielded. Sky emission in each order was modeled with a b-spline and was subtracted. Even in the near-infrared arm, sky emission could be well modeled in each exposure, without subtracting a noded frame. This procedure has the advantage of avoiding a  $\sqrt{2}$  penalty in the background noise. The reddest order ( $2.27\text{--}2.48 \mu\text{m}$ ) had to be nod-subtracted. The resulting signal-to-noise in the last order is lower than in the rest of the spectrum and the relative flux normalization

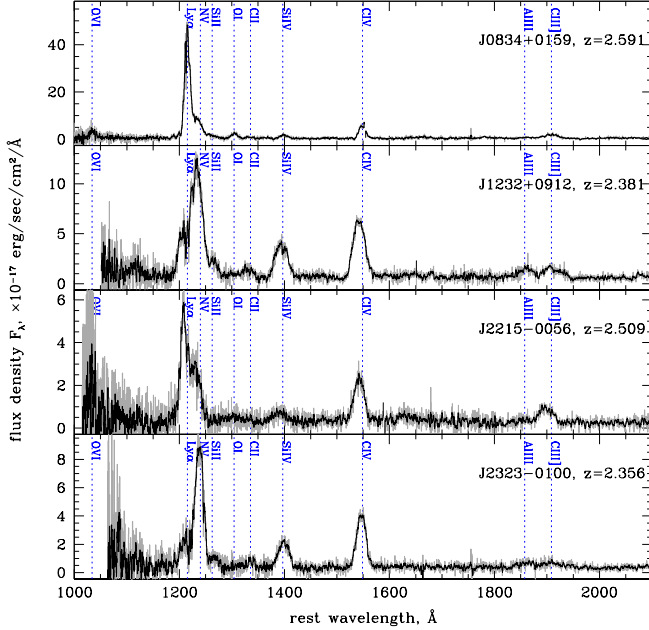


FIG. 1.— SDSS / BOSS spectra of the four extremely red quasars with extreme forbidden-line kinematics discovered in follow-up near-infrared observations (grey: unsmoothed, black: smoothed with 5-bin boxcar filter). The spectra are corrected to the rest frame of the sources using BOSS pipeline redshifts, as indicated in each panel. We use these redshifts throughout the paper, keeping in mind that the true rest-frame of the sources may not be well determined by the redshifts of the emission lines which may be subject to strong outflow signatures.

between that order and the rest of the spectrum is uncertain. The residual sky emission was modeled with a b-spline. Median per-pixel uncertainties resulting from the pipeline are in good agreement (within 30%) with the standard deviation of data around a linear continuum in a line-free region.

The counts in the two-dimensional frames were flux-calibrated using response curves generated from the observations of spectro-photometric standard stars. A single one-dimensional spectrum was then extracted simultaneously across all the orders and all exposures of a single object, avoiding multiple rebinnings and minimizing the error correlation between adjacent pixels. The one-dimensional spectra were binned to have fixed-velocity pixels ( $19 \text{ km s}^{-1}$ ). The wavelengths are on the vacuum heliocentric system.

Telluric corrections were performed using MOLECFIT (Smette et al. 2015; Kausch et al. 2015). Because the targets were specifically selected in redshift to avoid an overlap between the major emission lines and the strong telluric absorption features, the effect of telluric corrections is small for most measurements. The only noticeable effect is in SDSS J0834+0159, where telluric corrections lead to a 60% increase in the measured  $[\text{OIII}]\lambda 5007\text{\AA}$  flux.

### 3. ANALYSIS OF SPECTRA AND SPECTRAL ENERGY DISTRIBUTIONS

#### 3.1. $[\text{OIII}]$ kinematics

Figure 2 shows our VLT spectra of four extremely red quasars. The extreme kinematics of the

$[\text{OIII}]\lambda\lambda 4959, 5007\text{\AA}$  emission lines are immediately apparent. Not only are the two lines of the  $[\text{OIII}]$  doublet blended together (which does occur occasionally in the most kinematically extreme quasars at  $z \lesssim 1$ , Zakamska & Greene 2014), the doublet is further blended with  $\text{H}\beta$ , which indicates that line-of-sight velocities of order several thousand  $\text{km s}^{-1}$  must be present.

In this section, we quantify the kinematics of the  $[\text{OIII}]$  emission. Ideally, the best way to measure velocities would be relative to the rest-frame of the host galaxy as measured by stellar absorption lines, but we see no such lines in our spectra – the optical and near-infrared spectra are likely dominated by the quasar. Therefore, as an initial approximation we adopt the nominal BOSS pipeline redshifts (listed in Table 1) which are obtained by cross-correlating the optical (rest-frame ultra-violet) spectra against pre-defined templates (Bolton et al. 2012; in our case, against a normal blue type 1 quasar template), but with an understanding that they are not necessarily accurate. We then measure all kinematics relative to that frame and discuss possible avenues for determining the absolute host galaxy frame later in this section.

With such extremely high velocities in the forbidden emission lines, the traditional use of line kinematics for quasar type determination (“narrow line” type 2 vs “broad line” type 1) is meaningless (Section 4.1). The more physically motivated question is whether  $[\text{OIII}]$  and  $\text{H}\beta$  have consistent kinematic structure, which might indicate that they are emitted in the same physical region. Therefore, for every object we explore two classes of emission line fits: (1) ‘kinematically tied’ fitting functions which assume the same kinematics for  $\text{H}\beta$  and each of the  $[\text{OIII}]$  lines, and (2) ‘kinematically distinct’, or ‘untied’, fitting functions in which  $\text{H}\beta$  is allowed to have different kinematic structure from the components of the  $[\text{OIII}]$  doublet. The components of the  $[\text{OIII}]$  doublet are always assumed to have the same kinematics and the  $F_\lambda$  amplitude ratio  $[\text{OIII}]\lambda 4959\text{\AA}/[\text{OIII}]\lambda 5007\text{\AA}$  of 0.337.

To determine the underlying continuum, we calculate the median flux in  $20\text{\AA}$ -wide windows centered at rest-frame  $4750\text{\AA}$  and  $5090\text{\AA}$ , then subtract a linear interpolation between these two points to obtain the  $[\text{OIII}]+\text{H}\beta$  emission-line blend. Using one-Gaussian fits, we find that fits with kinematically distinct  $[\text{OIII}]$  and  $\text{H}\beta$  are preferred for SDSS J0834+0159, SDSS J1232+0912, and SDSS J2323-0100, whereas for SDSS J2215-0056 there is no appreciable statistical or visual difference between tied and untied fits. Specifically, in SDSS J0834+0159, SDSS J1232+0912, and SDSS J2215-0056 the centroids of  $[\text{OIII}]$  (as measured from the single-Gaussian fits) are offset from centroids of  $\text{H}\beta$  by  $-1009$ ,  $-1907$  and  $-1545 \text{ km s}^{-1}$ , respectively (in SDSS J2215-0056, the offset is nominally measured at  $128 \text{ km s}^{-1}$ , which is consistent with 0 given the large line widths of all features). It is also clear from these crude fits that the kinematics of  $[\text{OIII}]$  are rather extreme, with velocity dispersions  $1580$ ,  $2002$ ,  $1272$  and  $1168 \text{ km s}^{-1}$  for the four objects. Single-Gaussian fits do not capture well the shape of the lines, and in relatively low signal-to-noise spectra such fits lead to an underestimate of the actual velocity width (Zakamska & Greene 2014).

All fits are improved by adding a second Gaussian



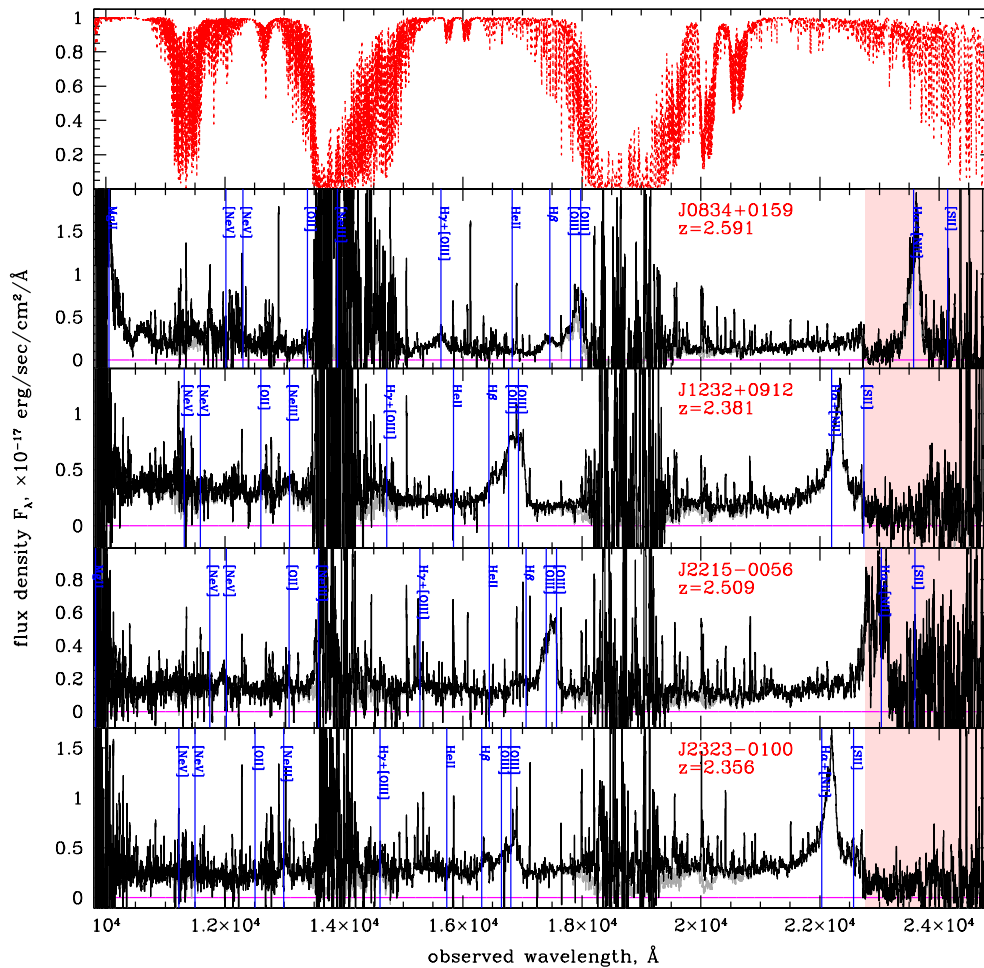


FIG. 2.— Top panel: atmospheric transmission curve for SDSSJ0834+0159. Bottom four panels: VLT spectra of the four extremely red quasars in this paper. Grey histogram shows extracted one-dimensional spectra smoothed with a 10-pixel boxcar, and black shows the telluric-corrected, 10-pixel-smoothed spectrum. The spectral regions of poor opacity correspond to the gaps between  $J$ ,  $H$  and  $K$  atmospheric bands, where the reconstructed spectrum has high noise. Blue vertical lines mark the expected locations of the major rest-frame-optical emission lines if the BOSS pipeline redshift is adopted at face value. The pink shaded region indicates the last order ( $\lambda > 22753\text{\AA}$ ) where the flux calibration relative to the rest of the spectrum is uncertain.

component (average reduced  $\chi^2$  improvement is 20%), and these fits are presented in Figure 3. The kinematically tied 2-Gaussian fits (shown in blue) assume that  $[\text{OIII}]\lambda 4959\text{\AA}$ ,  $[\text{OIII}]\lambda 5007\text{\AA}$  and  $\text{H}\beta$  have the same kinematic structure – i.e., all three lines have the same velocity offsets and velocity dispersions for each of the two Gaussian components and the same amplitude ratio of the two Gaussian components. The kinematically untied 2-Gaussian fits assume the same 2-Gaussian kinematic structure for  $[\text{OIII}]\lambda 4959\text{\AA}$  and  $[\text{OIII}]\lambda 5007\text{\AA}$ , but allow for a separate unconstrained single Gaussian for  $\text{H}\beta$ . Because of the relatively low signal-to-noise ratio of the  $\text{H}\beta$  detection alone, there is no statistical need for adding a second Gaussian component to  $\text{H}\beta$  in the kinematically untied fits.

The large apparent ratio of peaks of  $[\text{OIII}]\lambda 4959\text{\AA}$  and  $[\text{OIII}]\lambda 5007\text{\AA}$  – close to 1:1 in SDSS J1232+0912, compared to the theoretical ratio of 0.337 – implies that a strong broad blue-shifted component is required to fit the

$[\text{OIII}]$  doublet, which boosts the flux near the peak of  $[\text{OIII}]\lambda 4959\text{\AA}$ . In SDSS J0834+0159, SDSS J1232+0912, and SDSS J2323–0100 we find that kinematically untied fits produce a slightly better fit to the data; the main reason is that there is no evidence in the data for the broad blue component to the  $\text{H}\beta$  line of the kind that is clearly required to fit the  $[\text{OIII}]$  doublet. This is especially clear in SDSS J0834+0159, where the kinematically tied fit fails for the entire  $\text{H}\beta$  profile – both its blue and its red side. In SDSS J2215–0056 we find no statistically significant difference between kinematically tied and kinematically untied fits, so we prefer the kinematically tied fit for this object as the more simple model.

We do not assign any particular physical meaning to the parameters of the individual Gaussian components within the two-Gaussian fits for  $[\text{OIII}]$ . Rather, we use the fits to compute the non-parametric measures of the  $[\text{OIII}]\lambda 5007\text{\AA}$  profile, following Zakamska & Greene (2014) and many other authors. For any functional fit

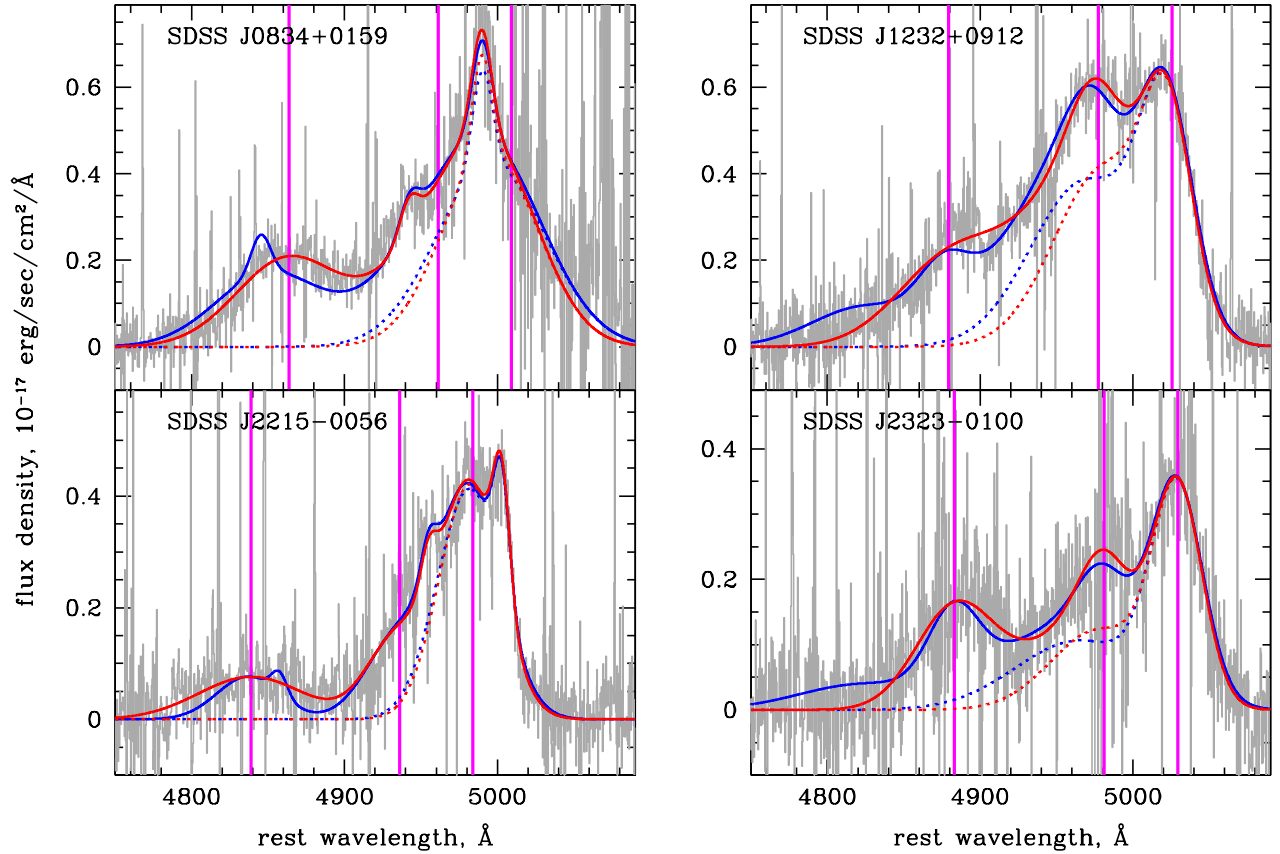


FIG. 3.— Fits to the  $H\beta$ + $[OIII]$  blend in the four extremely red quasars observed with VLT. A linear continuum anchored at 4750Å and 5090Å is subtracted before fitting. The blue solid line shows the best two-Gaussian, kinematically tied fit to the entire complex, whereas the red line assumes two Gaussian components for  $[OIII]$  and a single kinematically independent Gaussian for  $H\beta$ . The dotted lines display just the  $[OIII]\lambda 5007\text{\AA}$  profile for both fits. The solid magenta vertical lines mark the locations of  $H\beta$ ,  $[OIII]\lambda 4959\text{\AA}$  and  $[OIII]\lambda 5007\text{\AA}$  in the frame associated with the centroid of  $H\beta$  in the kinematically untied fit. The red line is our preferred fit for SDSS J0834+0159, SDSS J1232+0912 and SDSS J2323-0100, and the blue line is the preferred fit for SDSS J2215-0056 (in the latter case there is no statistical difference between the two fits, thus the one with the lower number of parameters is preferred).

to the  $[OIII]\lambda 5007\text{\AA}$  profile, we can calculate the velocity width comprising 90% of the flux  $w_{90}$  (and similarly  $w_{80}$ ) by rejecting the most extreme 5% blue-shifted and red-shifted parts of the profile. For a Gaussian profile, both are related to the velocity dispersion, with  $w_{80}$  being quite close to the commonly used full width at half maximum ( $w_{80} = 2.563\sigma_v = 1.088\text{FWHM}$ ;  $w_{90} = 3.290\sigma_v$ ). We list these measurements, together with full width at half maximum (FWHM) and full width at quarter maximum (FWQM) in Table 1.

The method is illustrated in Figure 4, where we display the best-fit  $[OIII]\lambda 5007\text{\AA}$  profiles in velocity space relative to the centroid of the  $H\beta$  determined from the kinematically untied fits. As measured relative to the frame of the  $H\beta$  centroid, median velocities  $v_{50}$  (in the order of increasing object right ascension) are  $-937$ ,  $-1520$ ,  $+79$ , and  $-769\text{ km s}^{-1}$ , i.e.,  $[OIII]$  is strongly blueshifted relative to the measured  $H\beta$  centroid in all but one case (SDSS J2215-0056). The velocity widths  $w_{80}$  range between 3600 and 5500  $\text{km s}^{-1}$ , FWHM between 2600 and 5000  $\text{km s}^{-1}$  and  $w_{90}$  between 4000 and 6700  $\text{km s}^{-1}$ . Such  $[OIII]$  widths are completely outside the

range found in type 1 quasars (Steinhardt & Silverman 2013; Shen 2015) and type 2 quasars at low redshifts (Zakamska & Greene 2014), as further discussed in Section 4.1. The peak signal-to-noise within the  $[OIII]$  doublet is  $\sim 10$  in our sources. If our assumptions about  $H\beta$  kinematics are correct, simulations conducted by Zakamska & Greene (2014) suggest that  $w_{80}$  and  $w_{90}$  are reliable for these values and accurate within  $\lesssim 15\%$  and that, if anything, these values would be underestimated in our sources because we may have missed another weak broad component.

$[OIII]$  can be artificially broadened by FeII contamination in unobscured quasars. While in obscured quasars FeII is not seen, we allow for the possibility that we see at least some nuclear continuum in our objects (whether scattered or directly penetrating through patchy obscuration; Section 3.4). To estimate the effect of FeII on our kinematic measurements, we use the Fe template from Boroson & Green (1992) which we convolve with a Gaussian function with the velocity dispersion of  $H\beta$ . Because the convolved templates show characteristic Fe blends centered at  $\sim 4600\text{\AA}$  and  $\sim 5300\text{\AA}$ , by looking

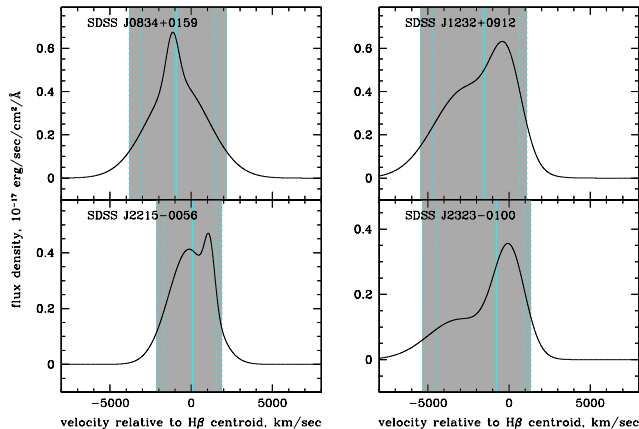


FIG. 4.— The best-fit profiles of  $[\text{OIII}]\lambda 5007\text{\AA}$  relative to the centroid of  $\text{H}\beta$ , shown in velocity space. Solid grey marks the part of the profile containing 90% of the line power ( $w_{90}$ ), whereas vertical cyan lines mark  $v_{05}$ ,  $v_{10}$ ,  $v_{90}$ ,  $v_{95}$  (dotted) and the median velocity of the profile  $v_{50}$  (solid).

at the maximal possible amplitudes of these features in the spectra we can subtract the maximal plausible Fe template from the data and remeasure the kinematics of the  $[\text{OIII}]+\text{H}\beta$  blend. We find that the line widths of  $[\text{OIII}]$  decrease by 10% in SDSS J2323–0100, 8% in SDSS J2215–0056 and 2% in SDSS J1232+0912, and increases by 8% in SDSS J0834+0159. We conclude that FeII does not severely affect the measured line kinematics. Furthermore, this allows us to estimate that the systematic uncertainties in our fits (e.g., due to continuum placement) are  $\lesssim 10\%$  for the kinematic measures presented in Table 1.

The FWHM of  $\text{H}\beta$  ranges between 3700 and 5000  $\text{km s}^{-1}$ . This is in the normal range for type 1 active nuclei and quasars (Hao et al. 2005; Steinhardt & Silverman 2013). Because of the specifics of our fitting routine, an extremely broad redshifted  $\text{H}\beta$  component would be fitted out as the blue-shifted component of  $[\text{OIII}]$ . Because we see no evidence for such component in  $\text{H}\alpha$  (Section 3.2), we find this scenario unlikely and we take the  $\text{H}\beta$  fit parameters at face value.

### 3.2. $[\text{NII}]$ and $\text{H}\alpha$

$[\text{NII}]\lambda\lambda 6548, 6583\text{\AA}$  and  $\text{H}\alpha$  are closer together in wavelength than  $[\text{OIII}]$  and  $\text{H}\beta$ , so disentangling their kinematics is even more complex. Therefore, we first attempt to fit this line blend with the best-fit kinematics of the  $[\text{OIII}]+\text{H}\beta$  blend. We assume that  $\text{H}\alpha$  has the same kinematics as  $\text{H}\beta$  (one-Gaussian fit) and that  $\text{H}\alpha$  flux is  $\geq 2.85 \times \text{H}\beta$  as required by the Case B recombination with allowance for reddening. Further, we assume that both  $[\text{NII}]$  lines have the same kinematics as  $[\text{OIII}]$  and that the peak  $F_\lambda$  ratio of  $[\text{NII}]\lambda 6548\text{\AA}$  to  $[\text{NII}]\lambda 6583\text{\AA}$  is 0.340. With these shape constraints, there are only two fitting parameters – the amplitudes of  $\text{H}\alpha$  and  $[\text{NII}]\lambda 6583\text{\AA}$ . In three cases where the noise is not prohibitively large, fits with these constraints fail in that they produce much more blue-shifted emission than what is observed (Figure 5). From this we conclude that the  $[\text{NII}]$  emission must be not nearly as blue-shifted and broad as  $[\text{OIII}]$  and thus likely arises from a different

spatial region in these quasars.

In SDSS J0834+0159, SDSS J1232+0912 and SDSS J2323–0100, we successfully fit the  $[\text{NII}]+\text{H}\alpha$  blend with a model that uses the same constraints on  $\text{H}\alpha$  as above (one-Gaussian kinematics fixed to that of  $\text{H}\beta$ , with Case B constraint on the minimal  $\text{H}\alpha$  flux) but allows for kinematics of  $[\text{NII}]$  independent from those of  $[\text{OIII}]$  (Table 1). One Gaussian component for  $[\text{NII}]$  is sufficient to produce adequate fits. In all three objects, the final  $\text{H}\alpha/\text{H}\beta$  ratio is consistent with Case B values, even though a larger ratio is allowed by the fit, and in fact without the lower bound the preferred  $\text{H}\alpha/\text{H}\beta$  ratios are smaller by as much as 50% than the Case B values (the most discrepant object is SDSS J0834+0159, where unfortunately the absolute flux calibration of the spectral region covering  $\text{H}\alpha$  is the most uncertain). One possible explanation is that in fact the true  $\text{H}\alpha/\text{H}\beta$  ratios are smaller than Case B, which is difficult (Gaskell & Ferland 1984), but not impossible (Korista & Goad 2004). Another possibility is that the kinematics of  $\text{H}\alpha$  are different from the kinematics of  $\text{H}\beta$ . A narrower  $\text{H}\alpha$  which is slightly redshifted relative to  $\text{H}\beta$  might improve the fits, but the blending of  $\text{H}\alpha$  with  $[\text{NII}]$  prevents us from testing such models.

With the exception of SDSS J2215–0056, where we consider  $[\text{NII}]$  to be non-detected, the best-fit  $[\text{NII}]$  lines are significantly narrower than the best-fit  $[\text{OIII}]$ . This is shown in Figure 6, where we use obscured quasars at  $z \lesssim 1$  with  $[\text{OII}]\lambda 3726, 3729\text{\AA}$  kinematics for comparison as the ionization potential of  $[\text{NII}]$  (14.5 eV) is similar to that of  $[\text{OII}]$  (13.6 eV). This observation is in line with studies demonstrating that lower ionization lines have more quiescent kinematics than do higher ionization ones (Whittle 1985b; De Robertis & Osterbrock 1986; Veilleux 1991).

The velocity centroids of  $[\text{NII}]$  (when fitted independently of  $[\text{OIII}]$ ) are offset by  $-100$  to  $300 \text{ km s}^{-1}$  from the centroids of  $\text{H}\alpha$  and  $\text{H}\beta$  (the measurement uncertainty in the centroid velocity is  $\lesssim 100 \text{ km s}^{-1}$ ), whereas in the same three objects the  $v_{50}$  centroids of  $[\text{OIII}]$  relative to the Balmer lines are between  $-800$  and  $-1500 \text{ km s}^{-1}$ . In the absence of the detection of the stellar absorption features, the centroids of the lowest-ionization forbidden emission lines are perhaps the best indicator of the host redshift. It is encouraging that the  $[\text{NII}]$  centroids are quite close to the Balmer centroids in the three objects. Although Balmer lines which originate close to the black hole may be affected by outflows (e.g., Flohic et al. 2012), kinematics of the disk around the black hole (e.g., Eracleous & Halpern 1994; Strateva et al. 2003) and gravitational redshifts (e.g., Tremaine et al. 2014), in practice they appear to be good proxies for the host redshifts.

### 3.3. Extreme $[\text{OIII}]\lambda 4363\text{\AA}$ in SDSS J0834+0159

SDSS J0834+0159 displays extraordinarily strong  $[\text{OIII}]\lambda 4363\text{\AA}$  emission (Figure 2). Because the  $[\text{OIII}]\lambda 4363\text{\AA}$  transition originates from a higher energy state than do  $[\text{OIII}]\lambda\lambda 4959, 5007\text{\AA}$ ,  $R_{[\text{OIII}]} \equiv (F_{4959} + F_{5007})/F_{4363}$  is a frequently used temperature diagnostic (Osterbrock 1989), normally ranging between 250 and 40 for temperatures between 10,000 K and 20,000 K and observed to be  $\sim 90$  in low-redshift obscured quasars

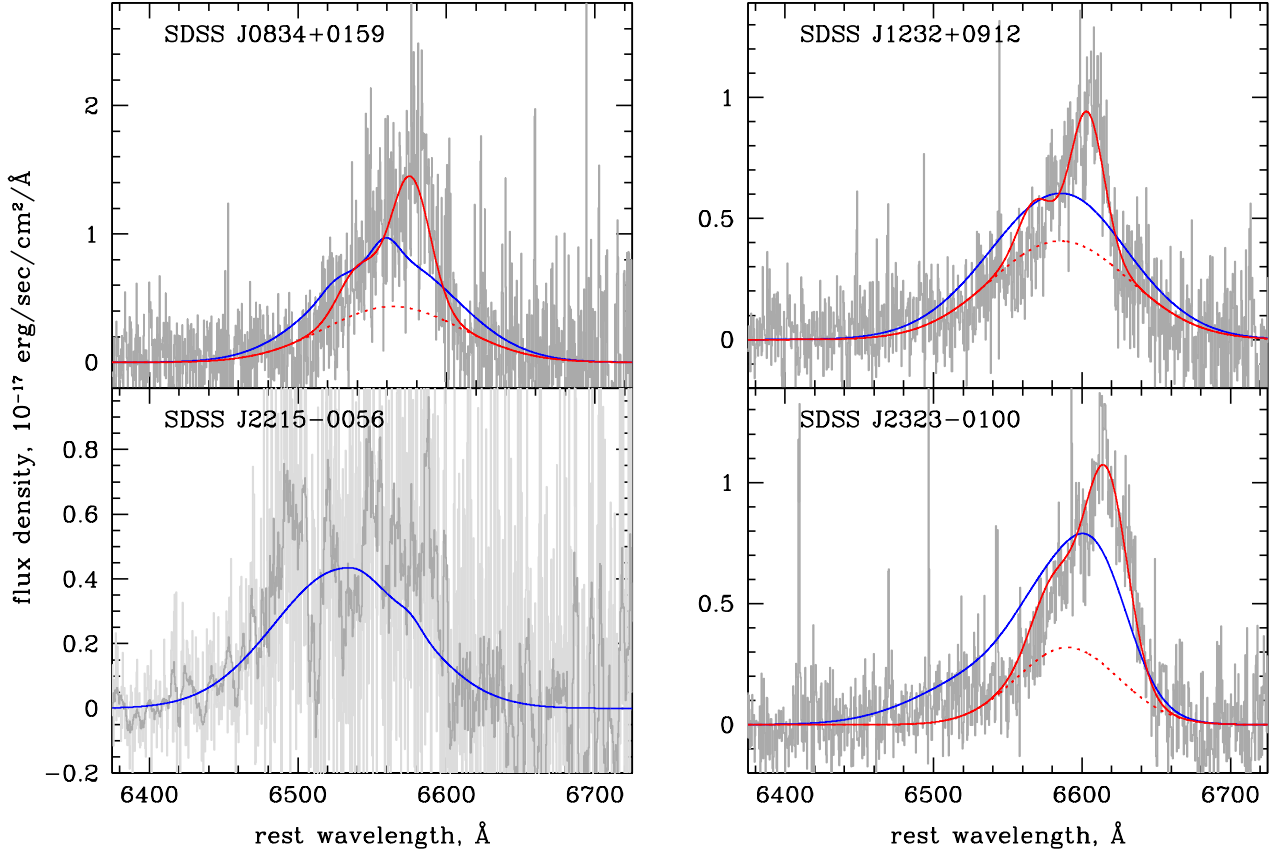


FIG. 5.— Fits to the  $H\alpha$ + $[NII]$  blends in the frame of the BOSS pipeline redshift, shown with linear continuum subtracted. We carry out two fits, both with  $H\alpha$  constrained to have the same shape as  $H\beta$ . In the first (blue), we tie the  $[NII]$  lines to the  $[OIII]$  profile, while in the second (red) the kinematics of  $[NII]$  are fit by a single Gaussian. Dotted lines show the contribution of  $H\alpha$  in the second fit. In SDSS J2215-0056, adding  $[NII]$  lines to the fit does not improve the  $\chi^2$  and we consider them undetected. In this object, light grey shows unbinned spectrum and dark grey the 10-pixel-binned one.

(Zakamska & Greene 2014). Given the extreme kinematics of the emission lines in this source,  $[OIII]\lambda 4363\text{\AA}$  is blended with  $H\gamma$  at  $4341\text{\AA}$ : the nominal velocity separation between the two lines is  $\sim 1500 \text{ km s}^{-1}$ , which is not sufficient to separate them out in this case. A precise measurement of  $R_{[OIII]}$  is therefore not possible, but we are able to recover robust lower and upper bounds as discussed below.

We try several approaches to deblending. In all fits we assume that the kinematics of  $H\gamma$  are the same as the kinematics of  $H\beta$ . We either fix  $H\gamma$  to its Case B value ( $H\gamma/H\beta=0.46$ ) or allow for a moderate extinction  $A_V \leq 2 \text{ mag}$  (even though no extinction is preferred by the  $H\alpha$  fit, the flux calibration of the longest wavelength order is uncertain enough that we do not fully rely on this measurement). As for  $[OIII]\lambda 4363\text{\AA}$ , we either fix its kinematics to those of  $[OIII]\lambda 5007\text{\AA}$  or fit it with a single Gaussian not kinematically constrained to any other lines.

As the total flux of the blend is fixed by the data, these assumptions provide us with a lower and an upper bound on the  $H\gamma$  flux and therefore on the upper and a lower bound on the  $[OIII]\lambda 4363\text{\AA}$  flux. Our resulting bounds

on  $R_{[OIII]}$  are  $13 \leq R_{[OIII]} \leq 39$ . What makes these values unusual is that for densities thought to be associated with the forbidden-line region of active galaxies,  $n_e \ll 10^5 \text{ cm}^{-3}$ , the derived range of  $R_{[OIII]}$  translates into the range of electron temperatures of  $20,000 \leq T_e \leq 64,000 \text{ K}$ , which is too high for a photo-ionized region in thermal balance (Osterbrock 1989; Baskin & Laor 2005). Another unusual detail is that there is some evidence for a difference in the kinematics of  $[OIII]\lambda 4363\text{\AA}$  and those of  $[OIII]\lambda 5007\text{\AA}$ . Specifically, fits with  $[OIII]\lambda 4363\text{\AA}$  kinematics fixed to those of  $[OIII]\lambda 5007\text{\AA}$  produce blue excess by comparison to the observed profile, and somewhat better fits are achieved with a less blueshifted ( $-750 \text{ km s}^{-1}$ ) and narrower ( $\sigma_v \lesssim 800 \text{ km s}^{-1}$ )  $[OIII]\lambda 4363\text{\AA}$ . Because of the strong blending, we consider this evidence tentative.

In light of the extreme  $[OIII]\lambda 5007\text{\AA}$  kinematics in our sources, one possible explanation for the relatively low  $R_{[OIII]}$  in SDSS J0834+0159 is contribution from fast shocks to the emission line ionization (Dopita & Sutherland 1995). It is then particularly intriguing that SDSS J0834+0159 displays a possible  $[OI]\lambda 6300\text{\AA}$  emission line (Figure 2), another feature



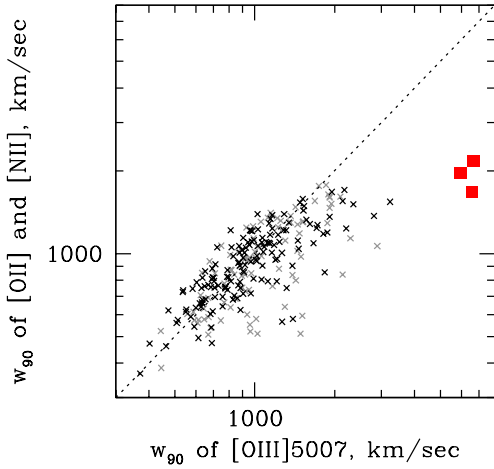


FIG. 6.— In low-redshift type 2 quasars, the  $[\text{OII}]\lambda\lambda 3726, 3729\text{\AA}$  doublet tends to be more kinematically quiescent than the  $[\text{OIII}]\lambda 5007$  emission line (black crosses for high signal-to-noise  $[\text{OII}]$  detections, grey for lower signal-to-noise ratio, data from Zakamska & Greene 2014). This trend is also seen in the  $[\text{NII}]\lambda 6583$  emission lines in our extremely red quasars (red squares). The measured  $[\text{OII}]$  widths have been corrected for doublet splitting as described by Zakamska & Greene (2014). The dotted line shows the 1:1 relation.

indicative of fast shocks. Alternatively, the low values of  $R_{[\text{OIII}]}$  may arise in regions of high electron density  $n_e \gtrsim 10^5 \text{ cm}^{-3}$  at modest temperatures  $< 20,000\text{K}$  (Baskin & Laor 2005). If this is the case, then  $[\text{OIII}]\lambda 5007\text{\AA}$  might primarily arise in less dense, more easily accelerated gas, whereas  $[\text{OIII}]\lambda 4363\text{\AA}$  arises in pockets of denser gas with higher inertia which are not as easily entrained by the wind, accounting for the difference in the observed kinematics.

With our current sample size and quality of the data we are unable to confidently detect  $[\text{OIII}]\lambda 4363\text{\AA}$  in other sources, though there may be hints for this line in SDSS J1232+0912 and SDSS J2323–0100. Unfortunately, in both cases the presence or absence of the feature is very sensitive to the assumed correction for the atmospheric transparency.

### 3.4. Spectral energy distributions

For every object, we select  $20\text{\AA}$ -wide emission-line-free windows centered at rest-frame 1460, 1700, 2000, 3300, 4700, and  $6200\text{\AA}$ . Using BOSS and VLT spectra we extract median fluxes at these wavelengths, which we consider to be pure continuum fluxes. We supplement those with WISE forced photometry (Lang et al. 2014) and show the continuum spectral energy distributions (SEDs) from optical to infrared wavelengths in Figure 7.

Our targets display high infrared-to-optical ratios (which reflects the initial selection criteria of the parent sample) with a characteristic steep rise of the SED from 1 to  $10\mu\text{m}$ . Of all quasar templates in the SWIRE library (Polletta et al. 2007) the only one that produces a similarly steep rise in the mid-infrared is the “torus” template derived from a high-redshift Compton-thick quasar (Polletta et al. 2006), shown in Figure 7 with a red curve. The remaining quasar templates in the SWIRE library all have lower infrared-

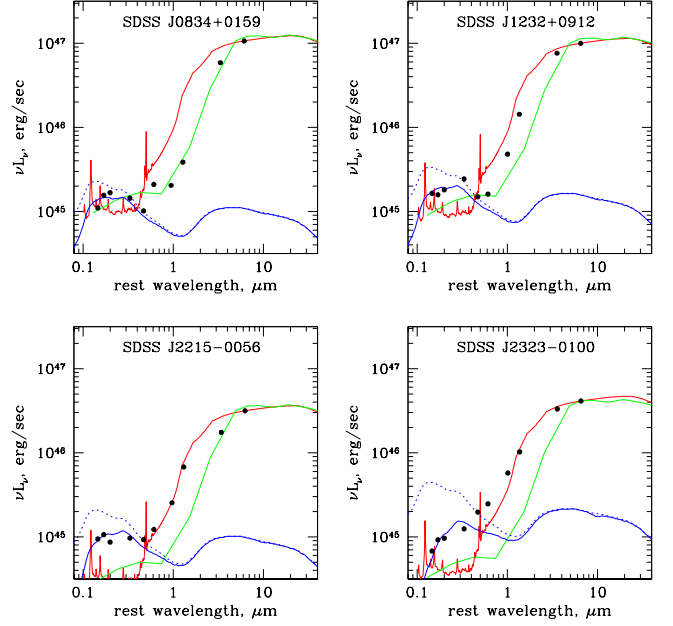


FIG. 7.— Continuum spectral energy distributions of our targets (black data points) assembled from BOSS spectra, VLT spectra and WISE forced photometry. For comparison, red lines show “torus” templates from Polletta et al. (2007) and green lines show HotDOG spectral energy distributions from Tsai et al. (2015), both normalized to the longest wavelength point. Optical and ultraviolet colors are inconsistent with those of unobscured quasars, with reddening by  $A_V = 0.6 - 2.5$  mag somewhat improving the agreement (solid blue lines: type 1 quasar template from Richards et al. 2006a affected by dust extinction from Weingartner & Draine 2001; dotted blue lines: templates with no extinction). The optical and ultraviolet fits are produced by quasars with bolometric luminosities  $L_{\text{bol}} \lesssim 10^{46} \text{ erg s}^{-1}$ , inadequate by at least an order of magnitude to explain the observed infrared emission.

to-optical ratios. The same characteristic shape in the mid-infrared is seen in hot dust-obscured galaxies (HotDOGs, Eisenhardt et al. 2012; Stern et al. 2014; Assef et al. 2015a; Piconcelli et al. 2015), whose average SED from Tsai et al. (2015) is shown with a green curve.

The apparent luminosities – calculated as total fluxes measured from ultraviolet to mid-infrared wavelengths, multiplied by  $4\pi D_L^2$  under the assumption that the emission is isotropic – are listed in Table 1, with a median of  $\sim 10^{46.8} \text{ erg s}^{-1}$ . The template luminosities – derived as the luminosities of the “torus” and HotDOG templates matched at the longest wavelength and also listed in Table 1 – are higher yet, with a median of  $10^{47.4} \text{ erg s}^{-1}$ , primarily because the templates allow us to make a guess as to the shape of the mid- and far-infrared SED and include it even though most of the infrared bump in the SED is not covered by the data. If obscuration makes any of the near- and mid-infrared emission anisotropic, as is suspected to be the case in low-redshift type 2 quasars (Liu et al. 2013b), then the true bolometric luminosities of our targets are even higher.

The extremely red quasars in our sample tend to have strong blue continua (necessary in order to be selected for follow-up spectroscopy in BOSS; Ross et al. 2012) with high-ionization emission lines being unambiguous signs of ionization by an active nucleus, whereas



HotDOGs have fainter optical continua often consistent with being due to stars in the host galaxy (Assef et al. 2015a). The median 2000Å continuum luminosity of our four sources is  $10^{45.1}$  erg s $^{-1}$ . Using Starburst99 (Leitherer et al. 1999) with calibration presented by Iglesias-Páramo et al. (2004), we find that this luminosity would require an unobscured star formation rate of  $2.6 \times 10^5 M_{\odot}$ /year, which is not a plausible explanation for the ultra-violet continuum flux of our sources. Even though the ultra-violet emission of our sources is suppressed by a factor of 30-100 compared to that of unobscured (type 1) quasars with matching mid-infrared luminosity (Fig. 7), it must be quasar-powered.

Hamann et al. (in prep. 2016a) present an extensive discussion of the possible origin of the peculiar optical-to-infrared properties of extremely red quasars. Briefly, extinction by a large-scale ( $\gg 1$  parsec) distribution of dust (including the toroidal obscuration of the classical unification model, Antonucci 1993) is not a good explanation for the observed spectral energy distribution of our sources because of the strong blue continuum. The overall shape of the ultraviolet / optical SED can be obtained by reddening an SED of an unobscured quasar by  $A_V \simeq 0.6$ – $2.5$  mag, but even correcting for reddening the ultraviolet and optical power is inadequate for producing the observed mid-infrared via absorption and thermal re-emission. The observed infrared-to-optical ratios are too high even in the case of a quasar obscured over virtually all of the sky, with narrow holes through the obscuration and with the observer happening by chance to see through one of those openings toward the entire continuum source: with typical optical luminosities of  $10^{45}$  erg s $^{-1}$  and bolometric corrections of  $\lesssim 10$  (Richards et al. 2006a), the observed optical luminosities fall an order of magnitude short of powering the observed infrared emission.

One possibility for reconciling the discrepancy between the optical and the infrared continua is that the optical and ultraviolet spectra of our sources are reprocessed by scattering. Even if the direct view to the quasar is obscured, light may be able to propagate through openings in the obscuring material, scatter off the interstellar medium in the host galaxy on scales greater than obscuration and reach the observer. This mechanism is responsible for the high polarization of obscured active galactic nuclei and quasars (e.g., Antonucci & Miller 1985; Zakamska et al. 2005). In our sources the required scattering efficiency would be 1 – 10%, which is plausible and in line with values seen in low-redshift obscured quasars (Zakamska et al. 2006; Obied et al. 2015). In this scenario the continuum and the Balmer lines seen in the VLT spectra are produced close to the quasar, but are seen only in reflected light, whereas forbidden lines are produced in a different physical region, perhaps a more extended one, explaining the differing kinematics of forbidden and permitted emission lines.

Another possibility is that the ultraviolet and optical continua are covered by a patchy screen of obscuring material, which lets only  $\lesssim 5\%$  of the light through, while largely preserving its spectral shape (Veilleux et al. 2013b). In order to provide partial covering of the ultraviolet continuum source which has sub-parsec size, the obscuring clouds must be individually even smaller and

therefore are likely to reside at the same sub-parsec physical scales where the continuum emission is produced. Thus the patchy obscuration scenario is different from the large-scale obscuration scenario ruled out above in that in the patchy obscuration case the observer sees only a fraction of the continuum luminosity whereas in the narrow opening case the observer would see the entire continuum source, but only with a small probability.

In both scenarios which are acceptable on the grounds of energetics – patchy obscuration and scattering – the equivalent widths of the emission lines produced close to the nucleus are expected to be unaffected. In the case of scattering, both the continuum emission and the line emission would be processed by a much more extended scatterer in the same way. In the case of patchy obscuration, the obscuring clouds must be present on the sub-parsec scale of the continuum emitter (Veilleux et al. 2013b), blocking ionizing photons that would otherwise be available for broad-line production and therefore again suppressing both the continuum and the line emission in the same way. The rest equivalent widths of H $\beta$  in our four sources (222, 86, 38 and 40Å) are roughly consistent with values found in type 1 quasars with the highest [OIII] luminosities (REW[H $\beta$ ] =  $96 \pm 29\%$  for  $L[\text{OIII}] > 10^{43.0}$  erg s $^{-1}$ , Shen et al. 2011), though the values in our sample show a large spread and their accuracy is  $\sim 30\%$  because of difficulties in continuum placement. Thus, if the observed H $\beta$  emission arises close to the black hole and not in the extended region which produces the [OIII] emission, the observed equivalent widths are consistent both with patchy obscuration and with scattering.

Assuming that underneath obscuration our sources are type 1 quasars with a typical spectral energy distribution and matching the observed infrared luminosities to the average quasar spectral energy distribution (Richards et al. 2006a), we estimate their optical luminosities to be  $\sim 10^{47}$  erg s $^{-1}$  or  $M_{2500} = -28.2$  mag, placing them among the top  $\sim 1\%$  most luminous quasars at this redshift (Richards et al. 2006b). Nonetheless, even at these extremely high luminosities unusually massive black holes are not required if the quasars are accreting at close to the Eddington limit ( $1.3 \times 10^{47}$  erg s $^{-1}$  for  $10^9 M_{\odot}$ ). While scattering and patchy obscuration might explain the overall shape of the SED (Assef et al. 2015b reach similar conclusions for HotDOGs), neither mechanism naturally explains the shapes and extremely high equivalent widths of ultraviolet emission lines and the extreme kinematics of [OIII] in our sources, so additional elements are required to explain the phenomenology of extremely red quasars in a self-consistent manner (Hamann et al. 2016a).

#### 4. DISCUSSION

##### 4.1. Comparison with other samples and type 1 / type 2 classification

In Figure 8, we compare the kinematics of the [OIII] in our objects against several other samples of red and obscured quasars. The [OIII] line widths seen in our sources are well above those seen in other samples of obscured and red quasars – for example, by a factor  $> 5$  in comparison with type 2 quasars at  $z < 1$ . The strong correlation between [OIII] kinematics and infrared luminosity was

already reported by Zakamska & Greene (2014), and the new observations reinforce the idea that more infrared-luminous quasars tend to produce higher velocity outflows, as the four objects lie on the extreme end of the infrared luminosity / line width correlation.

Traditionally, the observational distinction between type 1 (unobscured) and type 2 (obscured) active galaxies in the optical relied on the width of Balmer lines (Khachikian & Weedman 1974), with  $\text{FWHM}(\text{H}\beta) = 1200 \text{ km s}^{-1}$  (Hao et al. 2005) being a well-motivated criterion developed for low-luminosity active nuclei. While in these objects nuclear outflows are common (e.g., Crenshaw et al. 2003), they easily get stalled by the interaction with the interstellar medium and rarely result in kinematic disturbances of gas on larger scales, so [OIII] emission line profiles are dominated by gas moving in the Galactic potential (Wilson & Heckman 1985; Whittle 1992; Nelson & Whittle 1996; Greene & Ho 2005). But active galaxies at higher luminosities often show deviations from galaxy-supported [OIII] kinematics. For this reason, Zakamska et al. (2003), Reyes et al. (2008) and Alexandroff et al. (2013) expanded the search for obscured quasars to  $\text{FWHM}(\text{H}\beta) \leq 2000 \text{ km s}^{-1}$ . However, even with this higher cutoff some genuine type 2 quasars may be missed because forbidden lines alone (and therefore the part of the H $\beta$  emission coming from the same physical region) can be that broad (Nesvadba et al. 2008; Urrutia et al. 2012; Brusa et al. 2015). The [OIII] line profiles presented here for four extremely red quasars constitute perhaps the most extreme known examples.

As the [OIII] emission line widths enter squarely into the classical “broad-line” territory, the use of emission-line width for distinguishing obscured and unobscured quasars becomes increasingly problematic and new approaches are necessary. One approach (employed in Section 3.1) is to ask whether the forbidden and the permitted lines display the same kinematics (Reyes et al. 2008). If they do, this might support the ‘obscured’ classification because the lines arise in the same physical region, so there is no contribution to the permitted lines from high-density regions (presumably close to the black hole). We find that [OIII] and H $\beta$  kinematics are inconsistent in three objects and consistent in one, perhaps suggesting that in the former three the vicinity of the black hole is directly observed whereas in the latter it is not. Unfortunately, this standard is ambiguous: [OIII] and H $\beta$  kinematics can be strikingly different in known obscured quasars, especially in those with the strongest outflow signatures (Zakamska & Greene 2014), presumably due to the well-known but poorly understood stratification of the narrow-line region (e.g., Whittle 1985b; De Robertis & Osterbrock 1986; Veilleux 1991; Komossa et al. 2008).

Another possibility is to use the classical emission-line diagnostic diagrams (Baldwin et al. 1981; Veilleux & Osterbrock 1987). Emission from the broad-line region would contribute to H $\alpha$  and H $\beta$ , decreasing the apparent [OIII]/H $\beta$  and [NII]/H $\alpha$  ratios. None of our sources is close to the  $[\text{OIII}]\lambda 5007\text{\AA}/\text{H}\beta \sim 10$  value characteristic of the majority of obscured quasars at low redshifts (Zakamska & Greene 2014), which would indicate an additional contribution to Balmer lines and

thus a type 1 classification. Unfortunately, this method is also ambiguous, as the ionization conditions may be strongly modified by partial obscuration of the continuum and by the ram pressure of the winds (Stern et al. 2015), in which case low values of [OIII]/H $\beta$  can be naturally produced in the extended emission-line region. The rest equivalent widths of [OIII] which increase with stronger continuum obscuration are similarly ambiguous and are right in between type 1 and type 2 values (Greene et al. 2014b).

In Figure 9, we compare the infrared and [OIII] luminosities for several samples of obscured and unobscured active galaxies with those of our sources. [OIII] and infrared luminosities are strongly correlated in both obscured and unobscured quasars, supporting the idea that both can serve as measures of quasar luminosity. At a given [OIII] luminosity, type 1 quasars are about three times more infrared luminous than type 2 quasars:  $\nu L_\nu[13.5\mu\text{m}] = 10^{2.68} L[\text{OIII}]$  for type 1s, while the proportionality factor is  $10^{2.18}$  for type 2s. Most likely this is due to the fact that even at  $13.5\mu\text{m}$ , the thermal emission from obscured quasars is not isotropic. This can be seen both in theoretical models of quasar obscuration (Pier & Krolik 1992) and in SEDs of obscured quasars which are notably redder than type 1 SEDs even in the mid-infrared (Liu et al. 2013b).

The four extremely red quasars with median  $\log(\nu L_\nu[13.5\mu\text{m}]/L[\text{OIII}]) = 3.18$  lie an order of magnitude above the correlation for type 2 quasars (an appropriate comparison sample because of the similar shape of the SED), suggesting that [OIII] is suppressed by extinction by a factor of 10. The strong effect of dust extinction on [OIII] is also clear from the shape of the emission lines: the large overall blueshift of [OIII] is likely produced due to the extinction of the redshifted part of the outflow by the observer-facing (blue-shifted) part of the outflow (Heckman et al. 1981; De Robertis & Osterbrock 1984; Whittle 1985a; Wilson & Heckman 1985; Crenshaw et al. 2010). We offer this comparison with a caution that the extremely red quasar sample is infrared-selected and thus may have an infrared-to-[OIII] ratio biased somewhat high.

Another interesting possible connection is between our sources and the extreme end of the so-called Eigenvector 1 of the quasar population – unobscured AGNs with strong FeII, low [OIII]/H $\beta$  and relatively strong [OIII] blueshifts which are exemplified in the low-redshift universe by the so-called narrow-line Seyfert 1 galaxies (Boroson & Green 1992; Boroson 2002). Multiple lines of evidence suggest that Eigenvector 1 is driven by the increase in Eddington ratio (Wang et al. 1996; Laor et al. 1997; Wills et al. 1999) which we suspect is high in our targets based on their bolometric luminosity. At face value, our objects have neither strong FeII nor low [OIII]/H $\beta$  ratios, but that could be due to the suppression of the broad-line region by obscuration. However, both the blueshifts of [OIII] (extreme in our case, by comparison to those seen in low-redshift quasars, Boroson 2005) and the relatively low [OIII]/IR values may suggest some similarity with the Eigenvector 1 dominated objects. While this phenomenon is usually associated with relatively narrow H $\beta$  in the low-redshift universe, it is likely a luminosity effect (Sun & Shen 2015): as we

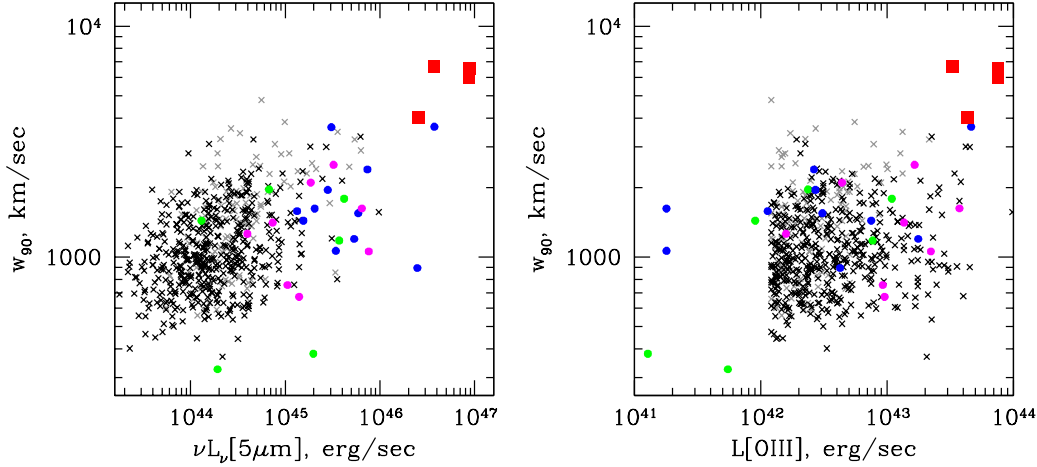


FIG. 8.— [OIII] kinematics as a function of mid-infrared luminosities and [OIII] luminosities for the four objects presented in this paper (red squares, median  $w_{90} = 6270 \text{ km s}^{-1}$ ) compared with those of other obscured and red quasar samples:  $z < 1$  type 2 quasars from Zakamska & Greene (2014) shown with grey and black crosses (black for peak signal-to-noise of [OIII]  $\gtrsim 20$ , grey otherwise; median  $w_{90} = 1060 \text{ km s}^{-1}$ ); X-ray selected obscured quasars at  $z \sim 1.0 - 1.5$  from Brusa et al. (2015) shown with green circles (median  $w_{90} = 1300 \text{ km s}^{-1}$ ); infrared-selected red quasars at  $z < 1$  from Urrutia et al. (2012) shown with blue circles (fitting parameters for [OIII] emission for these objects are published by Brusa et al. 2015; median  $w_{90} = 1580 \text{ km s}^{-1}$ ); and submm-selected  $z \sim 2$  active galaxies from Harrison et al. (2012) shown with magenta circles (median  $w_{90} = 1330 \text{ km s}^{-1}$ ). The sharp cutoff for black points in the right panel is a selection effect, as only objects with  $L[\text{OIII}] > 10^{8.5} L_{\odot}$  were analyzed by Zakamska & Greene (2014).

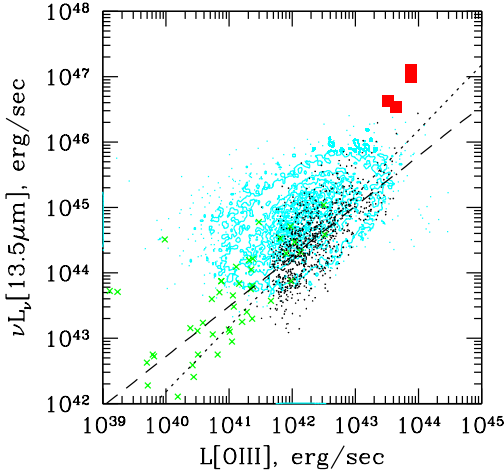


FIG. 9.— [OIII] and mid-infrared ( $13.5 \mu\text{m}$ ) luminosities for the four sources in this paper (red squares; top right two sources overlap so closely that they have been artificially offset from each other for clarity), for type 2 quasars at  $z < 0.8$  from Reyes et al. (2008) shown with black dots, for nearby Seyfert 2 galaxies from LaMassa et al. (2010) shown with green crosses, and for 17,000 type 1 quasars at  $z < 0.8$  from Shen et al. (2011) shown with cyan contours. The rest-frame  $13.5 \mu\text{m}$  luminosities of the four extremely red quasars in this paper are obtained from template fits shown in Figure 7. The dotted line fit to type 2 quasars and Seyfert 2s is made under the assumption that  $\nu L_{\nu}[13.5 \mu\text{m}] \propto L[\text{OIII}]$ , and we derive a coefficient of proportionality of  $10^{2.18}$ . The dashed line represents the best power-law fit.

have targeted very high luminosity sources, we probe higher black hole masses ( $\sim 10^9 M_{\odot}$ ) than those likely responsible for narrow-line Seyfert 1 objects ( $\sim 10^7 M_{\odot}$ ) and therefore we find  $\text{H}\beta$  widths to be in the normal range seen in type 1 quasars.

The extremely red quasars in our sample present with

a mix of type 1 / type 2 signatures which are likely due to a combination of patchy obscuration, scattering and extinction on nuclear scales and on the scales of the forbidden-line region. The standard line-width quasar type distinctions do not work in the regime of extreme outflow activity, and it is likely that the geometry and degree of obscuration in these sources are significantly different from the classical toroidal obscuration of the unification model (Antonucci 1993). Perhaps ultimately all these properties may be explained in the context of dusty winds radiatively driven during accretion at a high Eddington ratio (Thompson et al. 2015; Chan & Krolik 2015).

#### 4.2. Energetics

To calculate the energy of the outflow we need its mass and its velocity. We start by relating the observed velocity profiles with physical velocities of outflowing gas. We consider a spherically symmetric outflow with gas clouds moving radially away from the quasar with a distribution function  $f(v_r)dv_r$ , proportional to the luminosity emitted by gas with radial velocities between  $v_r$  and  $v_r + dv_r$ . The observed distribution of line-of-sight velocities  $v_z$  is then

$$F(v_z) \propto \int_0^1 \frac{da}{a} f\left(\frac{|v_z|}{a}\right), \quad (1)$$

where integration over  $a \equiv \cos \theta$  (where  $\theta$  is the angle between a streamline and a line of sight) takes into account projection effects and the solid angle of the gas seen at a given  $\theta$ . The mean radial velocity of clouds within the outflow is  $\langle v_r \rangle = \int_0^\infty v_r f(v_r) dv_r / \int_0^\infty f(v_r) dv_r$ . Regardless of the distribution function  $f(v_r)$ , the mean physical velocity has a remarkably simple relationship with the observable line-of-sight value  $v_z$ :

$$\langle v_r \rangle = 2 \langle |v_z| \rangle. \quad (2)$$



Thus given an observed line profile, one can calculate  $\langle |v_z| \rangle$  from observations and determine the average physical velocity of outflowing gas.

The outflows in our extremely red quasars are affected by extinction and thus the spherically symmetric approximation is not directly applicable. To estimate  $\langle |v_z| \rangle$  from our data, we assume that extinction mostly affects the redshifted part and use only the profiles at  $v_z < 0$ . With this approach and using equation (2), we estimate average physical velocities of the outflow of  $\langle v_r \rangle \sim 3500, 4900, 2100$  and  $4500 \text{ km s}^{-1}$  in the four objects. Because obscuration more strongly affects the streamlines that are further away from the line of sight, these estimates are likely biased high. For example, the parts of the outflow propagating close to the plane of the sky which produce zero line-of-sight velocities could be suppressed by extinction of the observer-facing side of the outflow. As a result, in the discussion that follows we estimate that the physical outflow velocity is  $3000 \text{ km s}^{-1}$  for all objects except SDSS J2215–0056 where the kinematics are less dramatic.

A standard method of estimating the kinetic energy of the ionized gas is to use recombination lines to estimate the mass of the emitting hydrogen (Nesvadba et al. 2006). It is not clear that we have detected the Balmer lines originating in the extended emission-line region (Section 4.1), but the data are consistent with  $[\text{OIII}]/\text{H}\beta = 10$  in the extended region and an additional contribution to  $\text{H}\beta$  from near the black hole. If we do assume this ratio for the moving gas, then we estimate

$$E_{\text{kin}} = 9.6 \times 10^{58} \text{ erg} \times \left( \frac{[\text{OIII}]/\text{H}\beta}{10} \right)^{-1} \left( \frac{L[\text{OIII}]}{10^{47} \text{ erg s}^{-1}} \right) \frac{\langle v^2 \rangle}{(3000 \text{ km s}^{-1})^2} \left( \frac{n_e}{100 \text{ cm}^{-3}} \right)^{-1} \quad (3)$$

#### 4.3. Physical scale of the [OIII] emission

If photo-ionization by the quasar is the dominant ionizing process, then narrow-line ratios (Dopita et al. 2002) and equivalent widths (Baskin & Laor 2005) suggest that most of the [OIII] emission originates in a region with ionization parameter  $U \equiv \Phi/4\pi cr^2 n_H(r) = 10^{-3} - 10^{-2}$ . If the ionization conditions producing forbidden emission lines in extremely red quasars are similar to those found in less extreme active galaxies, and if [OIII] is produced in regions with densities less than the critical density  $n_H < 8 \times 10^5 \text{ cm}^{-3}$ , then we arrive at the minimal size of the [OIII]-emitting region (Hamann et al. 2011):

$$R = 0.5 \text{ kpc} \times \left( \frac{\nu L_\nu[1450 \text{ \AA}]}{10^{47} \text{ erg s}^{-1}} \right)^{1/2} \left( \frac{n_H}{8 \times 10^5 \text{ cm}^{-3}} \right)^{-1/2} \left( \frac{U}{0.003} \right)^{-1/2} \quad (4)$$

For comparison, the broad-line region for a black hole with mass  $\sim 10^9 M_\odot$  is concentrated on scales  $\lesssim 1 \text{ pc}$ . Thus if the physics of [OIII] excitation is similar to that seen in nearby active galaxies, the high (suspected) intrinsic luminosity of extremely red quasars implies that the [OIII] emission must originate on scales comparable to the size of the host galaxy. For a more typical density of  $10^3 \text{ cm}^{-3}$  (Baskin & Laor 2005), the nominal emitting size is  $14 \text{ kpc}$ . Radiation-pressure-dominated models (Dopita et al. 2002; Stern et al. 2015) suggest somewhat higher ionization parameters, between  $U = 0.01 - 0.1$ ,

but even in this case the emitting size is between  $2.5$  and  $8 \text{ kpc}$ .

We can now combine the kinetic energy estimate from equation (3) with a size estimate to calculate the efficiency of conversion of the quasar luminosity into the kinetic energy of its wind. If  $\tau$  is the characteristic time scale of the outflow (for example,  $10^6$  years is the travel time to get to  $3 \text{ kpc}$  at  $3000 \text{ km s}^{-1}$ ), then the efficiency is

$$\eta_{\text{wind}} = \frac{E_{\text{kin}}}{L_{\text{bol}} \tau} = 3\% \times \left( \frac{E_{\text{kin}}}{10^{59} \text{ erg}} \right)^{-1} \left( \frac{L_{\text{bol}}}{10^{47} \text{ erg s}^{-1}} \right) \left( \frac{v}{3000 \text{ km s}^{-1}} \right) \left( \frac{R}{3 \text{ kpc}} \right)^{-1} \quad (5)$$

Such efficiencies are in the ballpark of those required by galaxy formation models for suppressing excessive growth of massive galaxies (Hopkins et al. 2006).

Normally shock ionization is energetically subdominant to photo-ionization in quasars (Stern et al. 2015). But in our objects, with their extreme kinematics, the possibility of shock ionization should be reconsidered in future analyses, especially with the indirect evidence for shocks supplied by strong  $[\text{OIII}]\lambda 4363 \text{ \AA}$  (Section 3.3).

#### 4.4. Acceleration mechanisms

How can large-scale gas in a galaxy be accelerated to such high velocities? Acceleration by radiation pressure on dust is usually assumed to produce winds that move with velocities just above the escape velocity (Thompson et al. 2015). As discussed in Section 4.3, we suspect that the [OIII] emission is produced on  $\gtrsim 1 \text{ kpc}$  scales, where the outflow velocities deduced from the [OIII] line shapes ( $v \sim 3000 \text{ km s}^{-1}$ ) are much greater than the local escape velocity (no more than a few hundred  $\text{km s}^{-1}$ ).

Thompson et al. (2015) recently re-examined the case of acceleration by radiation pressure of dusty winds which are optically thick in the ultra-violet and concluded that much higher velocities, with a significant momentum boost, may be reached because the clouds or shells experience radiation pressure over the entire time they remain optically thick. We use their calculation of the terminal velocity of dusty winds,  $v_\infty \simeq (4R_{\text{UV}}L/M_{\text{sh}}c)^{1/2}$ , where in our objects we estimate that  $v_\infty \simeq 3000 \text{ km s}^{-1}$ ,  $L \simeq 10^{47} \text{ erg s}^{-1}$  is the luminosity of the source,  $M_{\text{sh}}$  is the mass of accelerated dusty shells and  $R_{\text{UV}}$  is the distance from the source where the shell becomes optically thin to ultra-violet photons. This distance is unknown in our objects, but we estimate it by remarking that [OIII] emission, despite originating on  $\gtrsim 1 \text{ kpc}$  scales, shows signs of significant obscuration, both in its shape (strong blue excess) and in the total luminosity (Section 4.1). Therefore, we assume that the dusty, partially ionized clouds that produce [OIII] are still optically thick to ultra-violet emission at  $1 \text{ kpc}$  from the quasar and estimate that  $R_{\text{UV}} \gtrsim 3 \text{ kpc}$ . Then for the mass of the shell, we find:

$$M_{\text{sh}} = 6.9 \times 10^8 M_\odot \times \left( \frac{R_{\text{UV}}}{3 \text{ kpc}} \right) \left( \frac{L}{10^{47} \text{ erg s}^{-1}} \right) \left( \frac{v_\infty}{3000 \text{ km s}^{-1}} \right)^{-2}, \quad (6)$$



its kinetic energy is  $E_{\text{kin}} = 2R_{\text{UV}}L/c = 6.2 \times 10^{58}$  erg and its momentum boost (the ratio of the momentum of the shell to the momentum of the absorbed photons) is  $\dot{M}v_{\infty}c/L \simeq M_{\text{sh}}v_{\infty}^2c/(R_{\text{UV}}L) = 4$ . This kinetic energy is close to the estimate of the energy of the outflowing gas presented in Section 4.2 which is based on the [OIII] luminosity, suggesting that dust acceleration is an energetically plausible mechanism in our case.

An alternative possibility is that of light, ultra-fast ( $v \gtrsim 10,000$  km s $^{-1}$ ) radiatively-driven winds (Murray et al. 1995; Proga et al. 2000; Tombesi et al. 2015) which then collide with the interstellar medium of the surrounding host and shock and accelerate it to produce a galaxy-wide wind (King et al. 2011; Faucher-Giguère & Quataert 2012), with the quasar photo-ionizing the resulting wind (perhaps with additional ionization contribution from shocks themselves). When the wind is first initiated by the quasar, the high inertia of the surrounding gas allows for a build-up of pressure within the central few tens of pc as the quasar continues depositing the energy into this region via the wind. When the pressure builds up to sufficiently high levels, the pressure force can overcome the inertia of the surrounding material and drive an energy-conserving flow.

## 5. CONCLUSIONS

Extremely red quasars at  $z \sim 2.5$  discussed in this paper were first identified by their red optical-to-infrared colors, while at the same time showing unambiguous signs of quasar activity in their optical (rest-frame ultra-violet) spectra such as strong CIV $\lambda$ 1549Å (Ross et al. 2015). The infrared luminosities of these sources directly measured from WISE fluxes reach  $10^{47}$  erg s $^{-1}$ , placing them among the most luminous quasars known. These objects tend to display unusual ultra-violet emission line ratios – with NV $\lambda$ 1240Å/Ly $\alpha > 1$  in some cases – and stubby shapes of CIV $\lambda$ 1549Å, lacking the extended wings characteristic of lines in ordinary quasars (Hamann et al. 2016a).

In this paper we present near-infrared (rest-frame optical) follow-up observations of four of these objects. We find extreme [OIII] kinematics in all 4 cases, where the [OIII] $\lambda$ 4959,5007Å lines are not only blended together, but are blended with H $\beta$  as well. Multiple kinematic measures are presented in Table 1; for example, the FWHM of [OIII] $\lambda$ 5007Å is between 2600 and 5000 km s $^{-1}$  and in 3 out of 4 objects, the line centroids are blueshifted relative to the H $\beta$  centroids by up to 1500 km s $^{-1}$ . All four objects lie on the extreme end of the correlation between the [OIII] kinematics and the infrared lumi-

nosity (Figure 8). The characteristic [OIII]-emitting gas velocities in our sources are 5–6 times higher than those seen in obscured quasars at  $z \lesssim 1$  (Zakamska & Greene 2014).

At these extreme velocities, the gas cannot be confined by any realistic galaxy potential and is thus likely to escape from the galaxy; we suggest that these objects may be signposts of the extreme “blow-out” phase of quasar feedback observed at the peak epoch of galaxy formation. Our energetics estimates suggest that at least a few per cent of the bolometric luminosity is converted into the kinetic energy of the outflowing ionized gas. Such feedback efficiency is in the range of values required from quasar feedback by galaxy formation models (Hopkins et al. 2006; Choi et al. 2012). The observed winds are dusty, as manifested by the strong line asymmetry and by an overall deficit of [OIII] relative to the amount expected based on the infrared luminosity. Although we cannot spatially resolve the outflows with our current data, we estimate that the [OIII]-emitting gas must be extended on scales of  $\gtrsim 3$  kpc and therefore the wind is progressing on galaxy-wide scales.

Although the infrared-to-optical colors suggest significant levels of obscuration, their spectral energy distributions are inconsistent with extinction by a foreground screen of dust, and the ultra-violet continua of these objects ( $\nu L_{\nu} \sim 10^{45}$  erg s $^{-1}$ ) are too strong to be due to the host galaxy. The most likely explanation is that we observe the continuum source through patchy obscuration or reprocessed by scattering in the interstellar medium of the host galaxy or perhaps in the dusty outflow itself.

Hamann et al. (2016a) demonstrate that extremely red quasars such as the ones we study here are likely more common than are hot dust-obscured galaxies (HotDOGs). HotDOGs, in turn, appear to be as common as type 1 quasars of the same bolometric luminosity (Assef et al. 2015a). If our subsequent observations demonstrate that the [OIII] kinematics we see in these four sources are common for the extremely red quasars, this would imply that the “blow-out” phase may be a common phase in evolution of extremely luminous quasars. Whether every massive galaxy undergoes a period of such luminous quasar activity is not yet known. But it is clear that with observed velocities and energetics of gas removal, such winds could have a profound impact on the evolution of galaxies in which they occur, in a direct manifestation of quasar feedback on their hosts.

NLZ is grateful to C.-A. Faucher-Giguère, J. Krolik, J. Stern, and T. Urrutya for discussions and suggestions that helped improve the paper, and to the Institute for Advanced Study for continued hospitality.

## REFERENCES

- Alam, S., Albareti, F. D., Allende Prieto, C., et al. 2015, *ApJS*, 219, 12
- Alexandroff, R., Strauss, M. A., Greene, J. E., et al. 2013, *MNRAS*, 435, 3306
- Antonucci, R. 1993, *ARA&A*, 31, 473
- Antonucci, R. R. J., & Miller, J. S. 1985, *ApJ*, 297, 621
- Arav, N., Moe, M., Costantini, E., et al. 2008, *ApJ*, 681, 954
- Assef, R. J., Eisenhardt, P. R. M., Stern, D., et al. 2015a, *ApJ*, 804, 27
- Assef, R. J., Walton, D. J., Brightman, M., et al. 2015b, *ArXiv e-print 1511.05155*
- Baldwin, J. A., Phillips, M. M., & Terlevich, R. 1981, *PASP*, 93, 5
- Baskin, A., & Laor, A. 2005, *MNRAS*, 356, 1029
- Becker, R. H., White, R. L., & Helfand, D. J. 1995, *ApJ*, 450, 559
- Bolton, A. S., Schlegel, D. J., Aubourg, É., et al. 2012, *AJ*, 144, 144
- Boroson, T. 2005, *AJ*, 130, 381
- Boroson, T. A. 2002, *ApJ*, 565, 78

- Borson, T. A., & Green, R. F. 1992, *ApJS*, 80, 109
- Boyle, B. J., & Terlevich, R. J. 1998, *MNRAS*, 293, L49
- Brusa, M., Bongiorno, A., Cresci, G., et al. 2015, *MNRAS*, 446, 2394
- Cano-Díaz, M., Maiolino, R., Marconi, A., et al. 2012, *A&A*, 537, L8
- Chan, C.-H., & Krolik, J. H. 2015, *ArXiv e-prints*
- Chartas, G., Saez, C., Brandt, W. N., Giustini, M., & Garmire, G. P. 2009, *ApJ*, 706, 644
- Choi, E., Ostriker, J. P., Naab, T., & Johansson, P. H. 2012, *ApJ*, 754, 125
- Crenshaw, D. M., Kraemer, S. B., & George, I. M. 2003, *ARA&A*, 41, 117
- Crenshaw, D. M., Schmitt, H. R., Kraemer, S. B., Mushotzky, R. F., & Dunn, J. P. 2010, *ApJ*, 708, 419
- Crichton, D., Gralla, M. B., Hall, K., et al. 2015, *MNRAS*, *submitted*; *ArXiv preprint* 1510.05656
- Croton, D. J., Springel, V., White, S. D. M., et al. 2006, *MNRAS*, 365, 11
- Dawson, K. S., Schlegel, D. J., & et al. 2013, *AJ*, 145, 10
- De Robertis, M. M., & Osterbrock, D. E. 1984, *ApJ*, 286, 171
- . 1986, *ApJ*, 301, 727
- Dopita, M. A., Groves, B. A., Sutherland, R. S., Binette, L., & Cecil, G. 2002, *ApJ*, 572, 753
- Dopita, M. A., & Sutherland, R. S. 1995, *ApJ*, 455, 468
- Eisenhardt, P. R. M., Wu, J., Tsai, C.-W., et al. 2012, *ApJ*, 755, 173
- Eisenstein, D. J., Weinberg, D. H., Agol, E., et al. 2011, *AJ*, 142, 72
- Eracleous, M., & Halpern, J. P. 1994, *ApJS*, 90, 1
- Faucher-Giguère, C.-A., & Quataert, E. 2012, *MNRAS*, 425, 605
- Ferrarese, L., & Merritt, D. 2000, *ApJ*, 539, L9
- Flohic, H. M. L. G., Eracleous, M., & Bogdanović, T. 2012, *ApJ*, 753, 133
- Gaskell, C. M., & Ferland, G. J. 1984, *PASP*, 96, 393
- Gebhardt, K., Bender, R., Bower, G., et al. 2000, *ApJ*, 539, L13
- Greene, J. E., & Ho, L. C. 2005, *ApJ*, 627, 721
- Greene, J. E., Pooley, D., Zakamska, N. L., Comerford, J. M., & Sun, A.-L. 2014a, *ApJ*, 788, 54
- Greene, J. E., Zakamska, N. L., Ho, L. C., & Barth, A. J. 2011, *ApJ*, 732, 9
- Greene, J. E., Alexandroff, R., Strauss, M. A., et al. 2014b, *ApJ*, 788, 91
- Gültekin, K., et al. 2009, *ApJ*, 698, 198
- Hainline, K. N., Hickox, R., Greene, J. E., Myers, A. D., & Zakamska, N. L. 2013, *ApJ*, 774, 145
- Hamann, F., Kanekar, N., Prochaska, J. X., et al. 2011, *MNRAS*, 410, 1957
- Hao, L., Strauss, M. A., Tremonti, C. A., et al. 2005, *AJ*, 129, 1783
- Harrison, C. M., Alexander, D. M., Mullaney, J. R., & Swinbank, A. M. 2014, *MNRAS*, 441, 3306
- Harrison, C. M., Alexander, D. M., Swinbank, A. M., et al. 2012, *MNRAS*, 426, 1073
- Heckman, T. M., Armus, L., & Miley, G. K. 1990, *ApJS*, 74, 833
- Heckman, T. M., Miley, G. K., van Breugel, W. J. M., & Butcher, H. R. 1981, *ApJ*, 247, 403
- Hopkins, P. F., Hernquist, L., Cox, T. J., et al. 2006, *ApJS*, 163, 1
- Hopkins, P. F., Hernquist, L., Cox, T. J., & Kereš, D. 2008, *ApJS*, 175, 356
- Iglesias-Páramo, J., Buat, V., Donas, J., Boselli, A., & Milliard, B. 2004, *A&A*, 419, 109
- Kausch, W., Noll, S., Smette, A., et al. 2015, *A&A*, 576, A78
- Kelson, D. D. 2003, *PASP*, 115, 688
- Khachikian, E. Y., & Weedman, D. W. 1974, *ApJ*, 192, 581
- King, A. R., Zubovas, K., & Power, C. 2011, *MNRAS*, 415, L6
- Komossa, S., Xu, D., Zhou, H., Storch-Bergmann, T., & Binette, L. 2008, *ApJ*, 680, 926
- Korista, K. T., & Goad, M. R. 2004, *ApJ*, 606, 749
- LaMassa, S. M., Heckman, T. M., Ptak, A., et al. 2010, *ApJ*, 720, 786
- Lang, D., Hogg, D. W., & Schlegel, D. J. 2014, *ArXiv e-prints*
- Laor, A., Fiore, F., Elvis, M., Wilkes, B. J., & McDowell, J. C. 1997, *ApJ*, 477, 93
- Leitherer, C., Schaerer, D., Goldader, J. D., et al. 1999, *ApJS*, 123, 3
- Liu, G., Zakamska, N. L., Greene, J. E., Nesvadba, N. P. H., & Liu, X. 2013a, *MNRAS*, 430, 2327
- . 2013b, *MNRAS*, 436, 2576
- Liu, X., Zakamska, N. L., Greene, J. E., et al. 2009, *ApJ*, 702, 1098
- Madau, P., & Dickinson, M. 2014, *ARA&A*, 52, 415
- Mullaney, J. R., Alexander, D. M., Fine, S., et al. 2013, *MNRAS*, 433, 622
- Murray, N., Chiang, J., Grossman, S. A., & Voit, G. M. 1995, *ApJ*, 451, 498
- Nardini, E., Reeves, J. N., Gofford, J., et al. 2015, *Science*, 347, 860
- Nelson, C. H., & Whittle, M. 1996, *ApJ*, 465, 96
- Nesvadba, N. P. H., Lehnert, M. D., De Breuck, C., Gilbert, A. M., & van Breugel, W. 2008, *A&A*, 491, 407
- Nesvadba, N. P. H., Lehnert, M. D., Eisenhauer, F., et al. 2006, *ApJ*, 650, 693
- Nesvadba, N. P. H., Boulanger, F., Salomé, P., et al. 2010, *A&A*, 521, A65
- Obied, G., Zakamska, N. L., Wylezalek, D., & Liu, G. 2015, *MNRAS*, *submitted*
- Ogle, P., Boulanger, F., Guillard, P., et al. 2010, *ApJ*, 724, 1193
- Osterbrock, D. E. 1989, *Astrophysics of gaseous nebulae and active galactic nuclei* (University Science Books)
- Piconcelli, E., Vignali, C., Bianchi, S., et al. 2015, *A&A*, 574, L9
- Pier, E. A., & Krolik, J. H. 1992, *ApJ*, 401, 99
- Polletta, M., Tajer, M., Maraschi, L., et al. 2007, *ApJ*, 663, 81
- Polletta, M. d. C., Wilkes, B. J., Siana, B., et al. 2006, *ApJ*, 642, 673
- Proga, D., Stone, J. M., & Kallman, T. R. 2000, *ApJ*, 543, 686
- Reyes, R., Zakamska, N. L., Strauss, M. A., et al. 2008, *AJ*, 136, 2373
- Richards, G. T., Lacy, M., Storrie-Lombardi, L. J., et al. 2006a, *ApJS*, 166, 470
- Richards, G. T., Strauss, M. A., Fan, X., et al. 2006b, *AJ*, 131, 2766
- Ross, N. P., Myers, A. D., Sheldon, E. S., et al. 2012, *ApJS*, 199, 3
- Ross, N. P., Hamann, F., Zakamska, N. L., et al. 2015, *MNRAS*, 453, 3932
- Rupke, D. S. N., & Veilleux, S. 2013a, *ApJ*, 775, L15
- . 2013b, *ApJ*, 768, 75
- Sanders, D. B., Soifer, B. T., Elias, J. H., et al. 1988, *ApJ*, 325, 74
- Shen, Y. 2015, *ArXiv e-print* 1512.00005
- Shen, Y., Richards, G. T., Strauss, M. A., et al. 2011, *ApJS*, 194, 45
- Silk, J., & Rees, M. J. 1998, *A&A*, 331, L1
- Smette, A., Sana, H., Noll, S., et al. 2015, *A&A*, 576, A77
- Spoon, H. W. W., & Holt, J. 2009, *ApJ*, 702, L42
- Springel, V., Di Matteo, T., & Hernquist, L. 2005, *MNRAS*, 361, 776
- Steinhardt, C. L., & Silverman, J. D. 2013, *PASJ*, 65, 82
- Stern, D., Lansbury, G. B., Assef, R. J., et al. 2014, *ApJ*, 794, 102
- Stern, J., Faucher-Giguère, C.-A., Zakamska, N. L., & Hennawi, J. F. 2015, *ApJ*, *submitted*; *ArXiv preprint* 1510.07690
- Stockton, A., & MacKenty, J. W. 1987, *ApJ*, 316, 584
- Strateva, I. V., Strauss, M. A., Hao, L., et al. 2003, *AJ*, 126, 1720
- Sun, A.-L., Greene, J. E., Zakamska, N. L., & Nesvadba, N. P. H. 2014, *ApJ*, 790, 160
- Sun, J., & Shen, Y. 2015, *ApJ*, 804, L15
- Tabor, G., & Binney, J. 1993, *MNRAS*, 263, 323
- Thompson, T. A., Fabian, A. C., Quataert, E., & Murray, N. 2015, *MNRAS*, 449, 147
- Thoul, A. A., & Weinberg, D. H. 1995, *ApJ*, 442, 480
- Tombesi, F., Cappi, M., Reeves, J. N., et al. 2013, *MNRAS*, 430, 1102
- Tombesi, F., Meléndez, M., Veilleux, S., et al. 2015, *Nature*, 519, 436
- Tremaine, S., Shen, Y., Liu, X., & Loeb, A. 2014, *ApJ*, 794, 49
- Tsai, C.-W., Eisenhardt, P. R. M., Wu, J., et al. 2015, *ApJ*, 805, 90
- Urrutia, T., Lacy, M., Spoon, H., et al. 2012, *ApJ*, 757, 125
- Veilleux, S. 1991, *ApJ*, 369, 331
- Veilleux, S., Cecil, G., & Bland-Hawthorn, J. 2005, *ARA&A*, 43, 769
- Veilleux, S., Cecil, G., Bland-Hawthorn, J., et al. 1994, *ApJ*, 433, 48
- Veilleux, S., & Osterbrock, D. E. 1987, *ApJS*, 63, 295

Veilleux, S., Meléndez, M., Sturm, E., et al. 2013a, ApJ, 776, 27  
 Veilleux, S., Trippe, M., Hamann, F., et al. 2013b, ApJ, 764, 15  
 Vernet, J., Dekker, H., D’Odorico, S., et al. 2011, A&A, 536, A105  
 Villar-Martín, M., Tadhunter, C., Humphrey, A., et al. 2011, MNRAS, 416, 262  
 Wang, T., Brinkmann, W., & Bergeron, J. 1996, A&A, 309, 81  
 Weingartner, J. C., & Draine, B. T. 2001, ApJ, 548, 296  
 Whittle, M. 1985a, MNRAS, 213, 1  
 —. 1985b, MNRAS, 216, 817  
 —. 1992, ApJ, 387, 109  
 Wills, B. J., Laor, A., Brotherton, M. S., et al. 1999, ApJ, 515, L53  
 Wilson, A. S., & Heckman, T. M. 1985, in Astrophysics of Active Galaxies and Quasi-Stellar Objects, ed. J. S. Miller, 39–109

Wright, E. L., Eisenhardt, P. R. M., Mainzer, A. K., et al. 2010, AJ, 140, 1868  
 York, D. G., et al. 2000, AJ, 120, 1579  
 Zakamska, N. L., & Greene, J. E. 2014, MNRAS, 442, 784  
 Zakamska, N. L., Strauss, M. A., Krolik, J. H., et al. 2003, AJ, 126, 2125  
 Zakamska, N. L., Schmidt, G. D., Smith, P. S., et al. 2005, AJ, 129, 1212  
 Zakamska, N. L., Strauss, M. A., Krolik, J. H., et al. 2006, AJ, 132, 1496

TABLE 1  
EMISSION LINE PARAMETERS

object name	SDSS J0834+0159	SDSS J1232+0912	SDSS J2215–0056	SDSS J2323–0100
object R.A.	08:34:48.48	12:32:41.73	22:15:24.00	23:23:26.17
object declination	+01:59:21.1	+09:12:09.3	−00:56:43.8	−01:00:33.1
initial (pipeline) redshift	2.591	2.381	2.509	2.356
H $\beta$ centroid, km s $^{-1}$	54	1036	−1465	1257
H $\beta$ velocity dispersion, km s $^{-1}$	2103	2119	2128	1564
log [ $L$ (H $\beta$ ) in erg s $^{-1}$ ]	43.54	43.40	42.89	43.14
[OIII] Gaussian component 1:				
peak $F_{\lambda}$ , 10 $^{-17}$ erg s $^{-1}$ /cm $^2$ /Å	0.444	0.432	0.413	0.322
central velocity rel. to H $\beta$ , km s $^{-1}$	−828	−150	−123	11
velocity dispersion, km s $^{-1}$	1872	951	1259	957
[OIII] Gaussian component 2:				
peak $F_{\lambda}$ , 10 $^{-17}$ erg s $^{-1}$ /cm $^2$ /Å	0.236	0.412	0.211	0.123
central velocity rel. to H $\beta$ , km s $^{-1}$	−1155	−2643	1140	−3060
velocity dispersion, km s $^{-1}$	381	1964	315	1903
H $\alpha$ /H $\beta$	(2.85)	(2.85)	(11.37)	(2.85)
[NII]6583Å/H $\alpha$	(0.671)	(0.333)	n/a	(1.077)
[NII] central velocity rel. to H $\beta$ , km s $^{-1}$	292	−115	n/a	238
[NII] velocity dispersion, km s $^{-1}$	599	509	n/a	660
$v_{50}$ , median vel. of [OIII] rel. to H $\beta$ , km s $^{-1}$	−937	−1520	79	−769
$w_{80}$ velocity width of [OIII], km s $^{-1}$	4576	5311	3554	5409
$w_{90}$ velocity width of [OIII], km s $^{-1}$	5970	6571	4005	6690
FWQM: full width at quarter maximum, km s $^{-1}$	5213	6785	4051	6172
FWHM: full width at half maximum, km s $^{-1}$	2811	4971	3057	2625
log [ $L$ ([OIII]) in erg s $^{-1}$ ]	43.88	43.88	43.64	43.52
log ( $L_{\text{apparent}}$ in erg s $^{-1}$ )	46.9	47.0	46.5	46.7
log ( $L_{\text{template},1}$ in erg s $^{-1}$ )	47.6	47.6	47.1	47.2
log ( $L_{\text{template},2}$ in erg s $^{-1}$ )	47.6	47.5	47.0	47.1
rest eq. width of [OIII] (in Å)	(485)	280	213	88
rest eq. width of H $\beta$ (in Å)	222	86	38	40
rest eq. width of H $\alpha$ (in Å)	(425)	(180)	(524)	(71)

NOTE. — Notes on values in parentheses:

In the fits, H $\alpha$ /H $\beta$  are fixed to Case B value of 2.85 in SDSS J0834+0159, SDSS J1232+0912, and SDSS J2323–0100, and therefore the line ratios and the equivalent widths are given in parentheses. The best fits with the same kinematics, but without the restriction on the amplitude, have H $\alpha$  fluxes lower by 50%, 19% and 1%, respectively. In SDSS J0834+0159 H $\alpha$  falls into the last order where the flux calibration is very uncertain, so H $\alpha$  flux should be considered only as an estimate. The value of rest equivalent width of [OIII] in SDSS J0834+0159 is poorly determined because the continuum is strongly affected by telluric absorption between  $H$  and  $K$  bands.

Notes on uncertainties:

Most kinematic parameters are given to more than necessary number of significant digits. The uncertainties in line fits are dominated by systematics such as continuum placement (including possible FeII contamination) and telluric corrections. Performing the fits with and without the telluric corrections and with and without the FeII contribution, we estimate that in single-Gaussian fits the line width (and consequently line luminosity) uncertainties are  $\lesssim 15\%$  and those in the centroid velocities are  $\lesssim 200$  km s $^{-1}$ . In double-Gaussian fits, the individual components can change more significantly, but these uncertainties still apply for the non-parametric widths and median velocities.